

Molecular Gas in NUClei of GALaxies (NUGA).

X. The Seyfert 2 galaxy NGC 3147

V. Casasola^{1,2,4}, F. Combes², S. García-Burillo³, L. K. Hunt⁴, S. León⁵, & A. J. Baker⁶

¹ Dipartimento di Astronomia, Università di Padova, Vicolo dell'Osservatorio 2, I-35122, Padova

² Observatoire de Paris, LERMA, 61 Av. de l'Observatoire, F-75014 Paris, France

³ Observatorio Astronómico Nacional (OAN), Alfonso XII, 3, 28014-Madrid, Spain

⁴ Istituto di Radioastronomia/INAF, Largo Enrico Fermi, 5, 50125 Firenze, Italy

⁵ Instituto de Astrofísica de Andalucía (CSIC), Camino Bajo de Huétor, 24, 18008 Granada, Spain

⁶ Dept. of Physics and Astronomy, Rutgers, the State Univ. of New Jersey, 136 Frelinghuysen Road, Piscataway, NJ 08854, USA

Received XXX 2008/ Accepted YYY 2008

Abstract. We present $^{12}\text{CO}(1-0)$ and $^{12}\text{CO}(2-1)$ observations of the SA(rs)bc Seyfert 2 galaxy NGC 3147, obtained with the IRAM interferometer at $1''.9 \times 1''.6$ and $1''.6 \times 1''.4$ resolutions, respectively. We have also observed the central region of NGC 3147 with the IRAM 30 m telescope (at resolutions of $22''$ and $12''$ for $^{12}\text{CO}(1-0)$ and $^{12}\text{CO}(2-1)$, respectively), in order to obtain complete sampling at low spatial frequencies. These observations have been made in the context of the NUClei of GALaxies (NUGA) project, aimed at the study of the different mechanisms for gas fueling of active galactic nuclei (AGN). A central peak seen mainly in $^{12}\text{CO}(2-1)$ and a ring-like structure at $r \simeq 10'' \sim 2$ kpc dominate the ^{12}CO maps. In $^{12}\text{CO}(1-0)$ an outer spiral at $r \simeq 20'' \sim 4$ kpc is also detected, not visible in $^{12}\text{CO}(2-1)$ emission because it falls outside the field-of-view of the primary beam. The average I_{21}/I_{10} line ratio is ~ 0.7 in temperature units over the region mapped in both lines, consistent with the optically thick emission expected in the nuclei of spiral galaxies. The kinematics of the molecular structures are quite regular, although there is evidence for local non-circular or streaming motions. We show that the molecular gas distribution is similar but not exactly identical to those of star formation tracers, i.e., infrared (*Spitzer*) and ultraviolet (*GALEX*) emission. This agreement is consistent with a scenario of steady, ongoing formation of stars from the molecular clouds at a rate of $\sim 1 M_{\odot} \text{ yr}^{-1}$ within the innermost 4 kpc in radius.

Using a near-infrared (NIR) image obtained with adaptive optics at the Canada-France-Hawaii Telescope (CFHT), we identify a weak bar in NGC 3147, which is classified as non-barred galaxy in the optical. We then compute the gravity torques exerted by this stellar bar on the gas. The torque is obtained first at each point in the map, and then azimuthally averaged with a weighting determined by the gas surface density traced by the CO emission. We find that the gas inside the inner CO ring is subject to a net negative torque and loses angular momentum. This is expected for gas at the ultra-harmonic resonance (UHR), just inside the corotation resonance of the stellar bar. In contrast, the gas outside corotation, in the spiral arms comprising the outer spiral structure, suffers positive torques and is driven outwards. We conclude that some molecular gas is presently flowing into the central region, since we find negative torques down to the resolution limit of our images.

Key words. galaxies: individual: NGC 3147 - galaxies: spiral - galaxies: active - galaxies: nuclei - galaxies: ISM - galaxies: kinematics and dynamics

1. Introduction

The NUClei of GALaxies (NUGA) project (García-Burillo et al. 2003) is an IRAM Plateau de Bure Interferometer (PdBI) survey of nearby active galaxies to map the distribution and dynamics of molecular gas in the inner 1 kpc at high spatial resolution ($\sim 0''.5 - 1''$, corresponding to $\sim 50 - 100$ pc), and to study the mechanisms for gas fueling of low-luminosity active galactic nuclei (AGNs).

Most galaxies possess central supermassive black holes (SMBHs), and gas accretion onto these black holes is the phenomenon usually invoked to explain nuclear activity in galaxies. However, even if most galaxies host black holes, the existence of nuclear activity is far from universal. It is not clear whether the main limiting factor is the global gas mass available for fueling the AGN or the mechanisms for efficiently removing the angular momentum of the gas.

The main and non-trivial problem linked to the fueling of AGN is the removal of angular momentum from the disk gas (e.g., Jogee 2006, and references therein), a process which can

Table 1. Fundamental parameters for NGC 3147.

Parameter	Value	References ^a
RA (J2000)	10 ^h 16 ^m 53.6 ^s	(1)
DEC (J2000)	73°24′03″	(1)
V_{hel}	2813 km s ⁻¹	(1)
RC3 Type	SA(rs)bc	(1)
T Hubble Type	3.88	(2)
Inclination	29.5°	(2)
Position Angle	150°	(2)
Distance	40.9 Mpc (1″ = 198 pc)	(1)
L_B	$4.3 \times 10^{10} L_{\odot}$	(3)
M_{HI}	$8.3 \times 10^8 M_{\odot}$	(3)
$M_{\text{dust}}(60 \text{ and } 100 \mu\text{m})$	$1.7 \times 10^6 M_{\odot}$	(3)
L_{FIR}	$3.4 \times 10^{10} L_{\odot}$	(4)

^a (1) NASA/IPAC Extragalactic Database (NED); (2) Lyon Extragalactic Database (LEDa); (3) Bettoni et al. (2003); (4) *IRAS* Catalog.

be accomplished through non-asymmetric perturbations. These can be perturbations of external origin, such as galaxy collisions, mergers, and mass accretion (Heckman et al. 1986), or of internal origin due to density waves, such as spirals or bars, and their gravity torques (e.g. Sakamoto et al. 1999; Combes 2001). In addition to primary bars, fueling processes can be associated with more localized phenomena, such as nested nuclear bars (e.g. Friedli & Martinet 1993), lopsidedness or $m = 1$ perturbations (e.g. Shu et al. 1990; García-Burillo et al. 2000), or warped nuclear disks (e.g. Schinnerer et al. 2000a,b).

Since molecular gas is the predominant phase of the interstellar medium (ISM) in the inner kiloparsec of spiral galaxies, the study of its morphology and dynamics represents an optimal possibility for investigating AGN fueling mechanisms and their link with circumnuclear star formation. In order to do this, high-resolution maps of molecular gas are needed. Previous CO single dish (Heckman et al. 1989; Young et al. 1995; Braine et al. 1993; Casoli et al. 1996; Vila-Vilaró et al. 1998) and interferometric (Sakamoto et al. 1999; Regan et al. 2001; Helfer et al. 2003) surveys have mapped the gas in galaxies with relatively low spatial resolution (4″ – 7″). Moreover, the majority of these surveys only included small numbers of AGN in their samples. This paper, dedicated to the galaxy NGC 3147, is the tenth of a series where results obtained for the galaxies in the NUGA sample are described on a case-by-case basis.

NGC 3147 ($D = 40.9 \text{ Mpc}$, $1'' = 198 \text{ pc}$, $H_0 = 75 \text{ km s}^{-1} \text{ Mpc}^{-1}$) is an isolated (Bettoni et al. 2003) Seyfert 2 galaxy (Ho et al. 1997) of Hubble morphological type SA(rs)bc. Both *ROSAT* (Roberts & Warwick 2000) and *Chandra* (Terashima & Wilson 2003) observations have shown that this galaxy possesses a pointlike nuclear X-ray source, which is presumed to be the location of the AGN. The 0.3–10 keV *Chandra* image reveals a bright, compact source surrounded by very faint, soft, and diffuse emission. The 2–10 keV core is clearly detected and confined to a region of 2″ in radius. Interferometric observations of the continuum emission

at cm wavelengths with MERLIN and the VLBA have also shown a pointlike nonthermal continuum source at the position of the nucleus of NGC 3147, coincident with the X-ray source (Ulvestad & Ho 2001; Krips et al. 2006, 2007a). Very recent optical and X-ray observations of the nuclear region of this galaxy suggest that NGC 3147 is the first “true” Seyfert 2 in the sense that it intrinsically lacks a broad-line region (Bianchi et al. 2008). Table 1 reports the fundamental characteristics of NGC 3147.

The structure of this paper is as follows. In Sect. 2, we describe our new observations of NGC 3147 and the literature data with which we compare them. In Sects. 3 and 4, we present the observational results, both single dish and interferometric, describing the principal properties of the molecular gas including its morphology, its kinematics, and its excitation. A comparison between the CO observations and those obtained at other wavelengths is given in Sect. 5. In Sect. 6, we describe the computation of the gravity torques exerted on the gas by a weak stellar bar that we have identified using a near-infrared (NIR) image. In Sect. 7, we discuss our principal observational and theoretical results, which are summarized in Sect. 8.

2. Observations

2.1. IRAM interferometric CO observations

We observed the $J = 1 - 0$ and $J = 2 - 1$ lines of ¹²CO in NGC 3147 using the IRAM PdBI in October 2004, with the array deployed in its ABCD configurations. The six 15 m antennae were equipped with dual-band SIS receivers yielding SSB receiver temperatures between 40 and 50 K at both frequencies. The precipitable water vapor ranged from 4 to 10 mm (i.e., giving opacities of $\sim 0.2 - 0.3$), resulting in system temperatures of approximately 200 – 300 K on average. The spectral correlators were centered at 114.197 GHz (2793.75 km s⁻¹) and 228.390 GHz (2793.27 km s⁻¹), respectively. The coordinates of the PdBI phase tracking center are given in Table 1 and correspond to the (6 cm VLBA) nuclear radio position of Nagar et al. (2002).

Data cubes with 256×256 pixels (0.46 pixel⁻¹ for ¹²CO(1-0) and 0.23 pixel⁻¹ for ¹²CO(2-1)) were created over a velocity interval of -240 km s⁻¹ to +240 km s⁻¹ in bins of 10 km s⁻¹. The images were reconstructed using the standard IRAM/GILDAS¹ software (Guilloteau & Lucas 2000) and restored with Gaussian beams of dimensions 1.8″ × 1.6″ (PA = 62°) at 115 GHz and 1.4″ × 1.2″ (PA = 61°) at 230 GHz. In the cleaned maps, the rms levels are 2 mJy beam⁻¹ and 4 mJy beam⁻¹ for the ¹²CO(1-0) and ¹²CO(2-1) lines, respectively (at a velocity resolution of 10 km s⁻¹). The conversion factors between intensity and brightness temperature are 32 K (Jy beam⁻¹)⁻¹ at 115 GHz and 14 K (Jy beam⁻¹)⁻¹ at 230 GHz.

A continuum point source is detected at both 3 mm and 1.3 mm. The continuum flux density is $5.2 \pm 0.2 \text{ mJy}$ at 3 mm and $2.2 \pm 0.4 \text{ mJy}$ at 1.3 mm. Both values are consistent with the synchrotron source detected at centimeter wavelengths for

¹ <http://www.iram.fr/IRAMFR/GILDAS/>

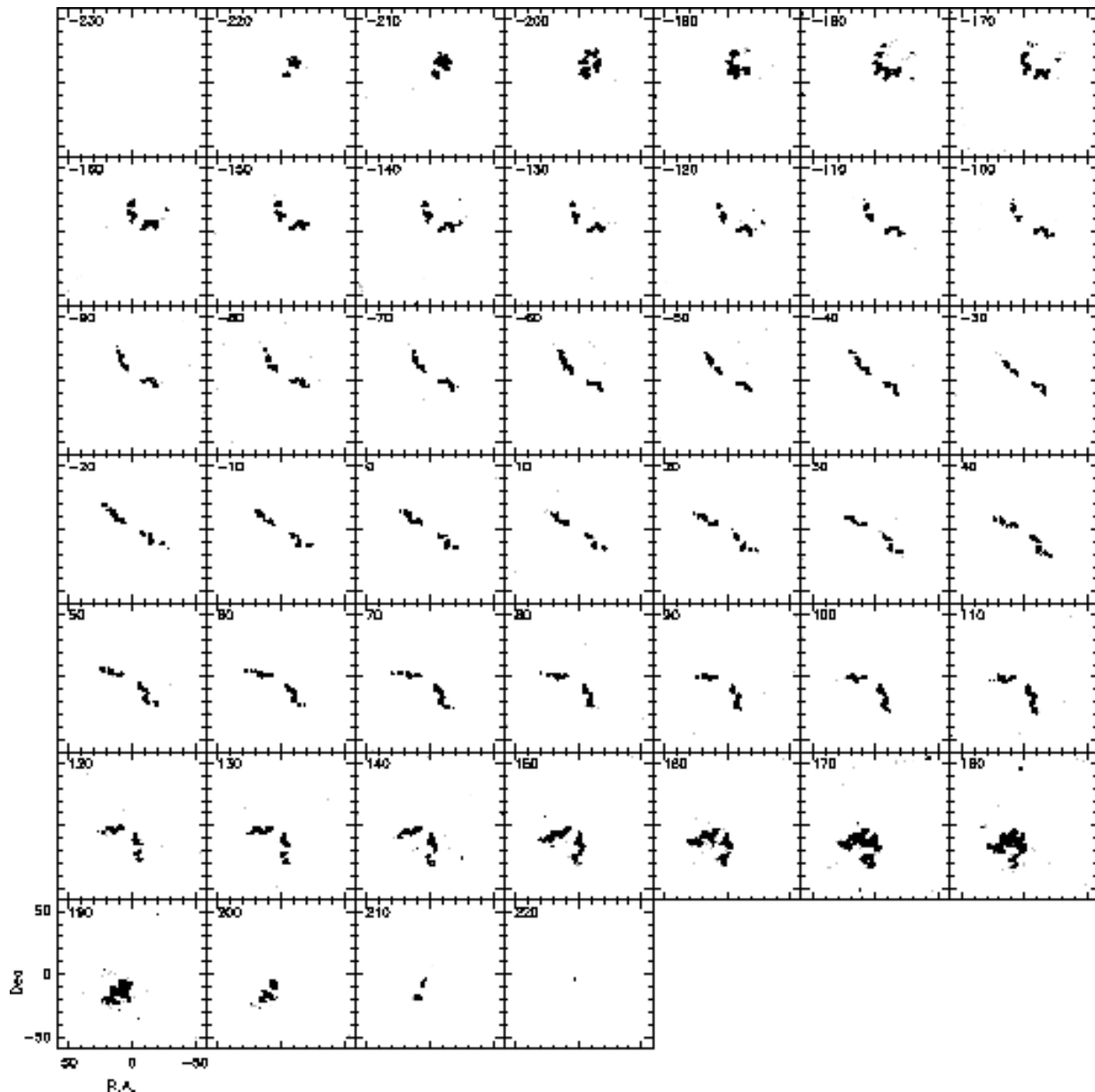


Fig. 1. $^{12}\text{CO}(1-0)$ velocity channel maps observed with the IRAM PdBI+30 m in the nucleus of NGC 3147, with a spatial resolution of $1''.9 \times 1''.6$ (HPBW). The center of the maps, given in Table 1, is $\alpha_{2000} = 10^{\text{h}}16^{\text{m}}53.6^{\text{s}}$, $\delta_{2000} = 73^{\circ}24'03''$. Velocity channels range from $\Delta V = -230 \text{ km s}^{-1}$ to $+220 \text{ km s}^{-1}$ in steps of 10 km s^{-1} relative to $V_{\text{hel}} = 2813 \text{ km s}^{-1}$. The contours begin at 5 mJy beam^{-1} , their spacing is 5 mJy beam^{-1} , and their maximum is 50 mJy beam^{-1} .

a power-law spectrum with a slope of -1 . All maps presented in the paper are continuum-subtracted.

2.2. IRAM single dish CO and HCN observations

We performed IRAM 30 m telescope observations in a 5×5 raster pattern with $7''$ spacing in July 2002 and in June 2004. We used 4 SIS receivers to observe simultaneously at the frequencies of the $^{12}\text{CO}(1-0)$ (115 GHz), the $^{12}\text{CO}(2-1)$ (230 GHz), and the HCN(1-0) (89 GHz) lines. The half power beam widths are $22''$ for $^{12}\text{CO}(1-0)$, $12''$ for $^{12}\text{CO}(2-1)$, and $29''$ for HCN(1-0). The typical system temperatures were $\sim 250 \text{ K}$ at 115 GHz, $\sim 350 - 700 \text{ K}$ at 230 GHz, and $\sim 120 \text{ K}$

at 89 GHz. The line intensity scale throughout this paper is expressed in units of T_{mb} , the beam-averaged radiation temperature. The value of T_{mb} is related to T_A^* , the equivalent antenna temperature (corrected for rear spillover and ohmic losses) reported above the atmosphere, by $\eta = T_A^*/T_{\text{mb}}$ where η is the telescope main-beam efficiency. η is 0.79 at 115 GHz, 0.57 at 230 GHz, and 0.82 at 89 GHz. All observations were performed in “wobbler-switching” mode, with a minimum phase time for spectral line observations of 2 s and a maximum beam throw of $240''$. The pointing accuracy was $\sim 3''$ rms.

Single dish observations were used to compute short-spacings and complete the interferometric measurements (e.g. Combes et al. 2004). In particular, short-spacing visibilities are

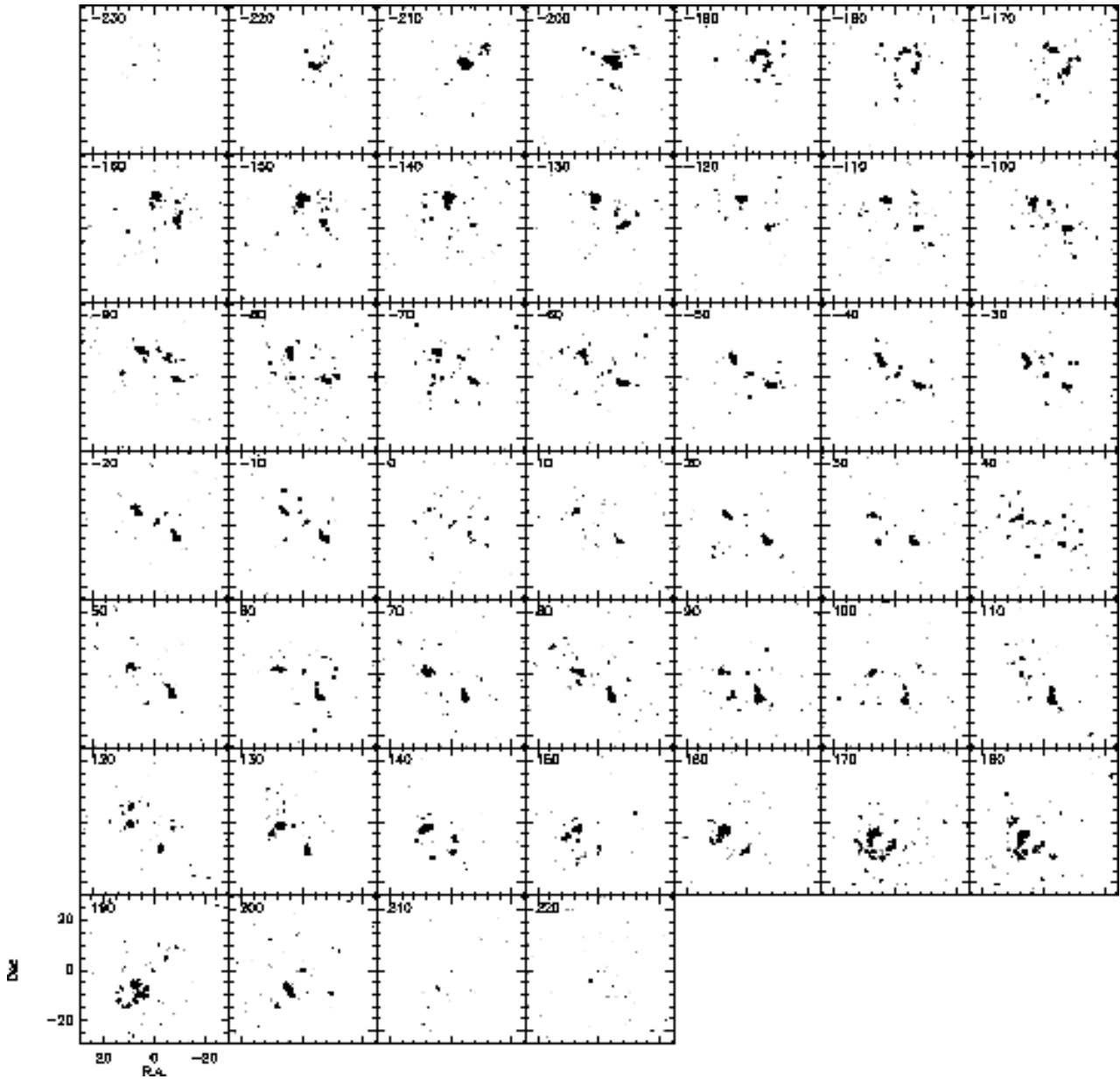


Fig. 2. Same as Fig. 1 but for the $^{12}\text{CO}(2-1)$ line, with a spatial resolution of $1''.6 \times 1''.4$. The velocity range is the same as for Fig. 1. The contours begin at 10 mJy beam^{-1} , their spacing is 5 mJy beam^{-1} , and their maximum is 45 mJy beam^{-1} .

computed from a map built by interpolation of the 30 m beam and multiplied by the PdBI primary beam. We combined 30 m and PdBI data, using the SHORT-SPACE task in the GILDAS software. To find the best compromise between good angular resolution and complete restoration of the missing extended flux, we varied the weights attached to the 30 m and PdBI data. After writing the combined datasets to visibility tables, converting to maps using standard data reduction procedures, and deconvolving using the Clark algorithm, we obtained maps with angular resolutions of $1''.88 \times 1''.63$ at PA 61.5° for the $^{12}\text{CO}(1-0)$ map and $1''.61 \times 1''.4$ at PA 65.4° for the $^{12}\text{CO}(2-1)$ map. The weights were adjusted in order to obtain the same mean weights in the single-dish data as in the interferometric data in the uv range of $1.25 D/\lambda$ to $2.5 D/\lambda$ ($D = 15 \text{ m}$). All

figures presented in this paper are made with short-spacing-corrected data.

Figs. 1 and 2 display the channel maps for the $^{12}\text{CO}(1-0)$ and $^{12}\text{CO}(2-1)$ lines, respectively. All maps are centered on the position of Table 1, and the dynamical center coincides with this center, which is also the position of the AGN (the radio continuum source).

Figs. 4 and 5 display the single dish data, for the $^{12}\text{CO}(1-0)$, $^{12}\text{CO}(2-1)$, and HCN(1-0) lines. The two CO lines have been mapped on a 5×5 grid with $7''$ spacings, while the HCN(1-0) line has been mapped on a 3×3 grid with $7''$ spacings and the nine HCN(1-0) spectra have been averaged to improve the signal-to-noise.

To estimate the flux filtered out by the interferometric observations, we have computed the flux measured by

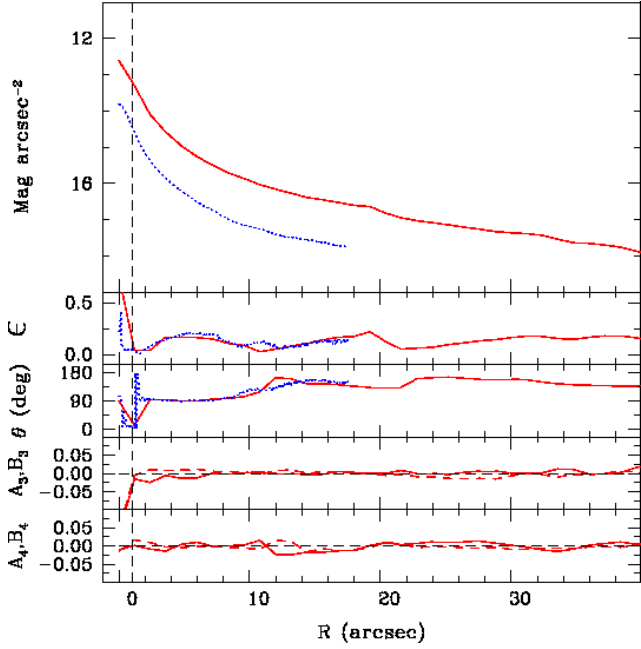


Fig. 3. Radial brightness profiles are shown in the top panel, with J given as a dotted line (blue), and IRAC $3.6\ \mu\text{m}$ as a solid one (red). The vertical dashed line corresponds to 200 pc. The lower panels display the radial runs of ellipticity, ϵ , position angle θ , and $\cos(4\theta)$ terms in the ellipse fitting residuals.

Young et al. (1995) with the FCRAO 14 m telescope (HPBW = $45''$). They found a $^{12}\text{CO}(1-0)$ intensity towards the center of $I(\text{CO}) = 5.75\ \text{K km s}^{-1}$ (in the T_A^* scale), which corresponds to an integrated flux of $S(\text{CO}) = 242\ \text{Jy km s}^{-1}$ if we adopt a conversion factor of $42\ \text{Jy K}^{-1}$. In the same region, we measure $130\ \text{Jy km s}^{-1}$ in $^{12}\text{CO}(1-0)$ with the PdBI alone, and $290\ \text{Jy km s}^{-1}$ with the IRAM 30 m in a beam of $22''$. With short-spacings added, we estimate the total flux to be $295\ \text{Jy km s}^{-1}$ in $^{12}\text{CO}(1-0)$, which is compatible with the FCRAO value within the uncertainties. In $^{12}\text{CO}(2-1)$, the PdBI alone indicates $30\ \text{Jy km s}^{-1}$ with a large region with negative flux levels. With the IRAM 30 m in $^{12}\text{CO}(2-1)$ we measure a total flux of $140\ \text{Jy km s}^{-1}$ in a beam of $12''$, and when short-spacings are included we recover the value of $151\ \text{Jy km s}^{-1}$.

The implication is that much of the $^{12}\text{CO}(2-1)$ emission comes from smoothly distributed gas.

2.3. Near-infrared observations

For modeling the gravitational potential, we used NIR images which have the advantage of being relatively free of dust extinction and more representative of old stellar populations than blue or visible images.

The NIR images were obtained in December 1998 at the 3.6 meter Canada-France-Hawaii Telescope (CFHT), using the CFHT Adaptive Optics Bonnette (AOB) and the KIR infrared camera. The AOB, also called PUEO after the sharp-visioned Hawaiian owl, delivers essentially diffraction-limited images at H and K' ($0''.11$ and $0''.14$, respectively), and images with FWHM $\sim 0''.1$ at J with guide stars as faint as $R = 14$ (see

Rigaut et al. 1998). Here the Seyfert nucleus of the galaxy was used for wavefront sensing. The KIR 1024×1024 pixel HgCdTe array has $0''.035/\text{pixel}$, providing a field of view of $36'' \times 36''$. The observations were obtained in excellent seeing conditions ($\sim 0''.6$ in the V band), with several images taken in a dithering procedure to correct for camera defects. The total on-source integration time was 8 minutes each for J and K' , and the total observing time for the two filters was 50 minutes including sky measurements and overheads.

A $J - K$ map was constructed by first subtracting sky emission, as estimated from the outer regions of the images. Then mean instrumental magnitude zero points were used to calculate a $J - K$ image, after aligning them to a common center.

2.4. Archival observations with Spitzer and GALEX

We acquired public images of NGC 3147 at other wavelengths to compare our molecular gas observations with other star formation tracers.

We used a far-ultraviolet (FUV) image from the *GALEX* satellite, whose band is centered at $\lambda_{\text{eff}} = 1516\ \text{\AA}$. This image has been already used and studied in the context of the *GALEX* Nearby Galaxies Survey (NGS, Gil de Paz et al. 2004; Bianchi et al. 2003a,b), a project that spans a large range of physical properties and morphological types of nearby galaxies. The image has been obtained with a total exposure time of 1693 s and covers a square region on the sky of size $\sim 5500'' \times 5500''$, i.e., much larger than the extent of the optical disk of NGC 3147, with $1''.5$ pixels. As the image was reduced with the *GALEX* data pipeline, it is already expressed in intensity units and sky-subtracted. The total FUV calibrated magnitude is 14.99 ± 0.01 , corresponding to a FUV flux density of $3669 \pm 17\ \mu\text{Jy}$.

We also acquired infrared (IR) images obtained with the IRAC camera on *Spitzer*, available thanks to the project ‘A Mid-IR Hubble Atlas of Galaxies’ (Principal Investigator: G. Fazio, see also Pahre et al. 2004). These images range in wavelength from $3.6\ \mu\text{m}$ to $8\ \mu\text{m}$, and were reduced with the *Spitzer* data pipeline (version S14.0.0). As in the case of the *GALEX* image, they cover a large sky area ($\sim 1400'' \times 700''$). These images have been rotated to canonical orientation (north up, east left) in order to allow correct superposition on the molecular gas map. The pixel size is $1''.20$ in the final images. The stellar component at $3.6\ \mu\text{m}$ and $4.5\ \mu\text{m}$ was subtracted from the $8.0\ \mu\text{m}$ image according to the prescriptions of Helou et al. (2004) and Pahre et al. (2004). This procedure provides a ‘‘dust-only’’ image at $8\ \mu\text{m}$, which we will discuss in Sect. 5.2.

Using the $3.6\ \mu\text{m}$ image, we calculated radial surface-brightness profiles by fitting ellipses (using the IRAF/STSDAS task *ellipse*). The center was fixed, but the ellipticity and the position angle were allowed to vary. This brightness profile is shown in Fig. 3, together with the J -band radial profile obtained in a similar way from the CFHT image. The zero point for the IRAC image was taken from the IRAC documentation at the *Spitzer* Science Center (<http://ssc.spitzer.caltech.edu/irac/calib/>).

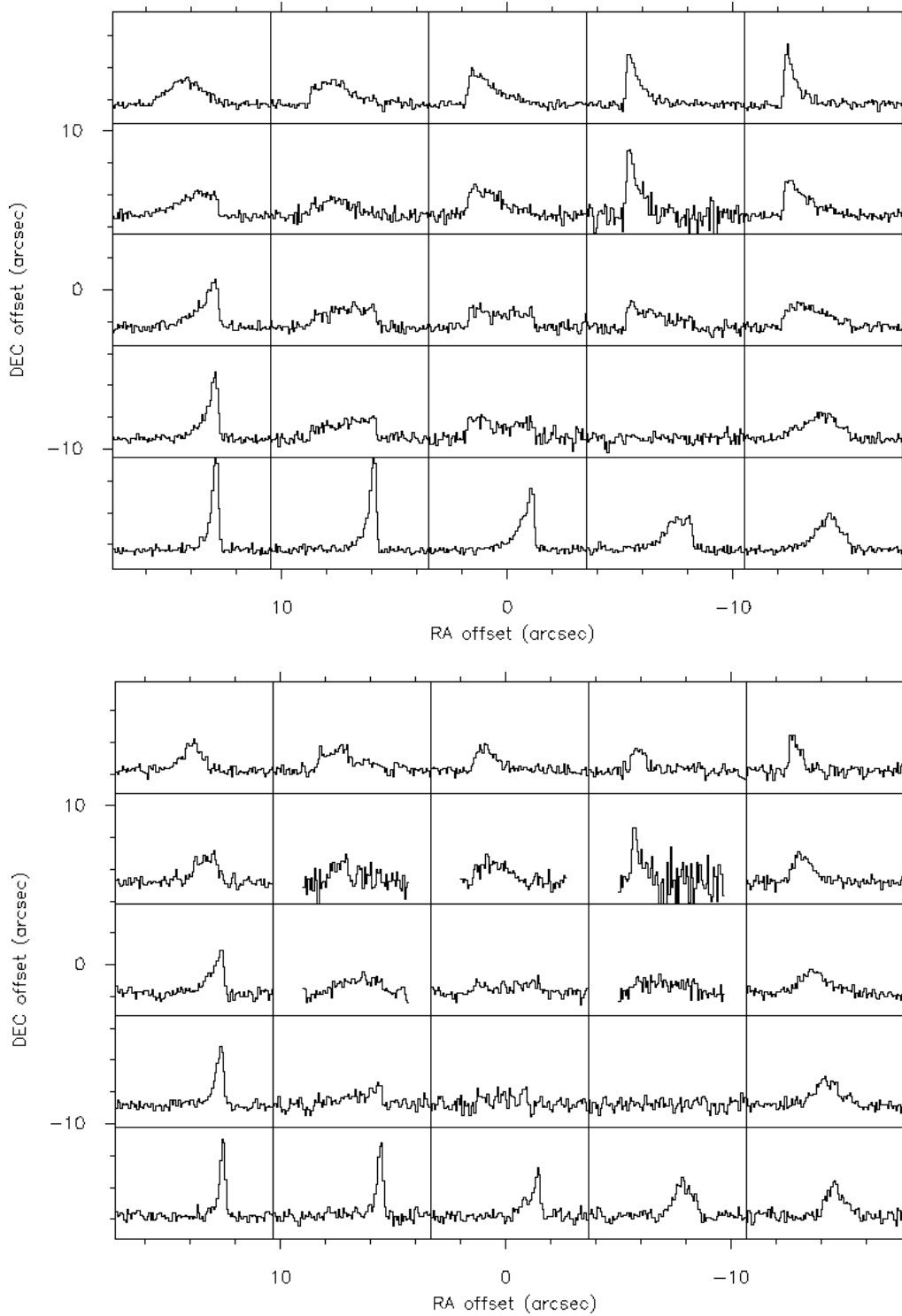


Fig. 4. Spectra maps of NGC 3147 made with the IRAM 30 m with $7''$ spacing in $^{12}\text{CO}(1-0)$ (top) and $^{12}\text{CO}(2-1)$ (bottom). The positions are offsets relative to the center of NGC 3147, whose coordinates are listed in Table 1. Each spectrum has a velocity scale from -500 to 500 km s^{-1} , and an antenna temperature scale (T_A^*) from -0.05 to 0.25 K for $^{12}\text{CO}(1-0)$ and to 0.20 K for $^{12}\text{CO}(2-1)$.

No corrections were made to the “standard” IRAC photometric calibrations.

Also shown are the runs of ellipticity, ellipse position angle, and $\cos(4\theta)$ residuals of the ellipse fitting. A local peak in the ellipticity profile at $R \approx 5''$ (1 kpc) at constant position an-

gle (85°) corresponds to a weak bar/oval feature that will be discussed in Sect. 5.1.

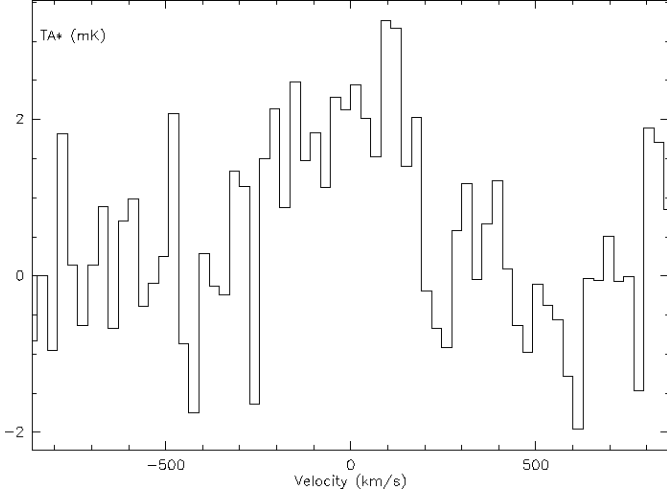


Fig. 5. HCN(1-0) spectrum towards the center of NGC 3147, averaged over the 9-point map made with the IRAM 30 m with 7'' spacing.

3. Single dish results

The observations performed with the A and B receivers of the IRAM 30 m telescope in the two ^{12}CO lines covered the central $\sim 50''$, corresponding to the central ~ 10 kpc (in diameter) of the galaxy (Fig. 4). The 25 observed positions show that the central region of NGC 3147 presents extended molecular emission in both $^{12}\text{CO}(1-0)$ and $^{12}\text{CO}(2-1)$ (Fig. 4). The maximum detected T_{mb} is 0.32 K in $^{12}\text{CO}(1-0)$ and 0.31 K in $^{12}\text{CO}(2-1)$, in the southeast region corresponding to the offsets ($10'', -10''$) and ($5'', -10''$) relative to the galaxy center.

The combination of observations of the $^{12}\text{CO}(1-0)$ and $^{12}\text{CO}(2-1)$ lines allowed us to compute the line ratio, $R_{21} = I_{21}/I_{10} = \int T_{mb}(2-1)dv / \int T_{mb}(1-0)dv$, an indicator of physical properties of the molecular gas such as excitation and optical depth. After smoothing the $^{12}\text{CO}(2-1)$ data to the $^{12}\text{CO}(1-0)$ beam resolution ($22''$) and correcting for the different beam efficiencies, we found a mean line ratio for the central region of NGC 3147 of 0.8. This value is consistent with the optically thick emission from molecular gas expected for the central regions of spiral galaxies (Braine & Combes 1992).

Assuming a CO- H_2 conversion factor $X = N(\text{H}_2)/I_{\text{CO}} = 2.2 \times 10^{20} \text{ cm}^{-2} (\text{K km s}^{-1})^{-1}$ (Solomon & Barrett 1991), the total H_2 mass derived from these single dish observations is $M_{\text{H}_2} = 8.2 \times 10^9 M_{\odot}$, within a radius of 5 kpc.

The HCN(1-0) line has been observed for 9 positions with 7'' spacing covering the central $43''$, corresponding to the central ~ 8.5 kpc (in diameter). The HCN(1-0) emission has been detected most significantly in the northwest part of the observed grid corresponding to the offset ($-7'', 7''$). The HCN(1-0) average spectrum over the 3×3 grid is plotted in Fig. 5. The CO(1-0)/HCN(1-0) ratio is equal to 20 on average. Because the observed region contains the AGN, we would expect enhanced HCN emission there. Hence, the observed CO(1-0)/HCN(1-0) ratio is unexpectedly high. For instance in NGC 1097, this ratio is 3 in the nucleus and 10 in the star-forming ring (Kohno et al. 2003). NGC 3147 is more similar to the starburst in NGC 6951

(Krips et al. 2007b), where the ratio is 30 in the ring, and 2.5 in the nucleus.

To study the physics and distribution of the molecular gas in detail we need to analyze both single dish and interferometric observations. The analysis in the remainder of the paper will be performed on the combined IRAM PdBI+30 m datasets.

4. Interferometric results: Molecular gas properties

4.1. Morphology and mass of the CO rings

The $^{12}\text{CO}(1-0)$ and $^{12}\text{CO}(2-1)$ integrated intensity distributions are shown in Fig. 6. The figure reveals a nuclear peak, a symmetric and complete inner ring at a distance of about $10''$ from the nucleus, and a larger and incomplete ring at a distance of about $20''$ from the nucleus (left panel). In $^{12}\text{CO}(2-1)$ the nuclear peak is stronger and more visible (right panel), but there is no outer ring at a radius of $20''$ because of the restricted field-of-view (FWHM of primary beam of $22''$). The outer ring-like structure can also be interpreted as spiral arms, more tightly wound in the inner regions than in the outer ones. The radial distribution of the azimuthally averaged $^{12}\text{CO}(1-0)$ and $^{12}\text{CO}(2-1)$ intensities is shown in Fig. 7, where there are clear dips between the central peak and the inner ring and between the inner ring and the outer spiral structure (partial outer ring).

Both $^{12}\text{CO}(1-0)$ structures are clumpy, composed of individual giant molecular cloud complexes, each with a mass of a few 10^7 to $10^8 M_{\odot}$. The total H_2 mass derived from the interferometer maps, assuming the same CO-to- H_2 conversion value used before, is $M_{\text{H}_2} = 3.8 \times 10^9 M_{\odot}$. The inner ring alone contributes more than half of the total masses; $M_{\text{H}_2} = 2 \times 10^9 M_{\odot}$, and the two parts of the outer spiral have similar mass, the western part has a mass of $M_{\text{H}_2} = 9.5 \times 10^8 M_{\odot}$ and the eastern one $M_{\text{H}_2} = 8.5 \times 10^8 M_{\odot}$. The total M_{H_2} ($= 3.8 \times 10^9 M_{\odot}$) we find is in good agreement with the mass derived by Young et al. (1995) for a position centered on the galaxy nucleus, $M_{\text{H}_2} = 4.4 \times 10^9 M_{\odot}$. Our mass estimate from single dish observations presented in Sect. 3 is larger, since it corresponds to a more extended region. In any case, this molecular gas mass is very large, more than three times larger than the most massive of the other NUGA galaxies studied so far (NGC 2782 and NGC 4569, see Hunt et al. 2008; Boone et al. 2007).

The comparison between the ^{12}CO maps of the two transitions, at the same resolution and with the same spatial frequency sampling, gives insight about the excitation conditions of the molecular gas locally, pixel by pixel. Fig. 8 shows that when the $^{12}\text{CO}(2-1)$ data are tapered and convolved to the $^{12}\text{CO}(1-0)$ resolution, the maxima of the $^{12}\text{CO}(2-1)$ ring agree quite well with the $^{12}\text{CO}(1-0)$ peaks. The ratio map is shown in Fig. 9 where the values range from 0.1 to 1.8. The mean ratio is ~ 0.7 , consistent with the value found with single dish observations and also, in this case, consistent with the bulk of emission being optically thick, as expected in the nuclei of spiral galaxies. Some regions, especially the center, reach a higher ratio (~ 1.3 - 1.4) where the gas is warm and dense, while in the disk and spiral arms it is colder and more diffuse. The peak in the northwest region of the CO(2-1)/CO(1-0) ratio map is co-

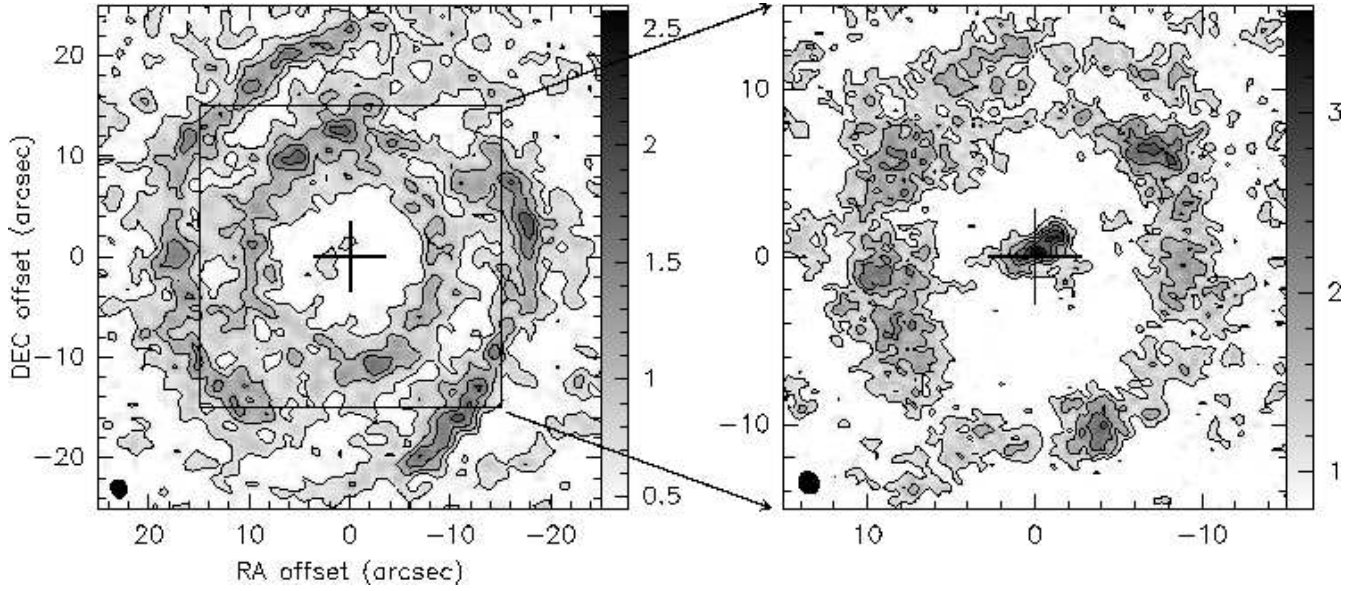


Fig. 6. *Left panel:* $^{12}\text{CO}(1-0)$ integrated intensity contours observed with the IRAM PdBI+30 m toward the center of NGC 3147. The cross marks the coordinates of the center as given in Table 1, with offsets in arcseconds. The rms noise level is $\sigma = 0.15 \text{ Jy beam}^{-1} \text{ km s}^{-1}$. The map, derived with 2σ clipping, has not been corrected for primary beam attenuation. Contour levels run from 4σ to 17σ with 2.5σ spacing. In this map the full $\pm 240 \text{ km s}^{-1}$ velocity range is used. The beam of $1''.9 \times 1''.6$ is plotted at lower left. *Right panel:* Same for $^{12}\text{CO}(2-1)$. The rms noise level is $\sigma = 0.2 \text{ Jy beam}^{-1} \text{ km s}^{-1}$. Contour levels run from 5σ to 18σ with 2.5σ spacing. The beam of $1''.4 \times 1''.2$ is plotted at lower left.

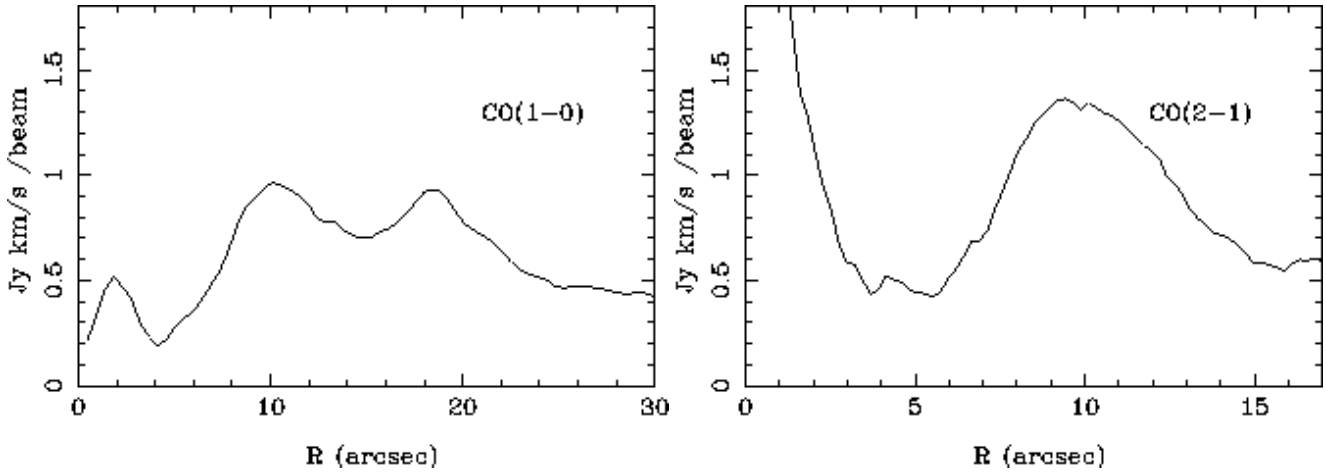


Fig. 7. *Left panel:* Radial distribution (azimuthal average, deprojected to face-on orientation) of the $^{12}\text{CO}(1-0)$ integrated intensity shown in Fig. 6. *Right panel:* Same for $^{12}\text{CO}(2-1)$.

incident with the strongest HCN(1-0) emission corresponding to the offset $(-7'', 7'')$.

4.2. Kinematics

The channel maps in Fig. 1 display overall a gross regularity of the large scale kinematics, following the expected spider diagram. However, there are some local wiggles superposed on this pattern, i.e., streaming motions. Such streaming motions are also visible in Fig. 10, which shows the isovelocity curves (first-moment map) of the $^{12}\text{CO}(1-0)$ emission superposed on the $^{12}\text{CO}(1-0)$ integrated intensity. Some of the perturbations

in the velocity field are clearly coincident with the spiral arms, as expected from density wave theory.

A position-velocity (p-v) cut along the major axis using a position angle of 150° is presented in Fig. 11. The major-axis p-v diagram shows approximately regular kinematics, although there are clear signs of deviations from “flatness” at $\sim 15''$ on either side of the nucleus of amplitude $\sim 40 \text{ km s}^{-1}$.

The minor-axis p-v diagram is displayed in Fig. 12. The wiggles are more conspicuous on the major axis in Fig. 11 than in Fig. 12. Although the minor-axis velocities are not completely symmetric about the nucleus, they hint that the outer spiral arm/pseudo-ring at a radius of $20''$ is already outside corotation. This is because the sign of the radial streaming

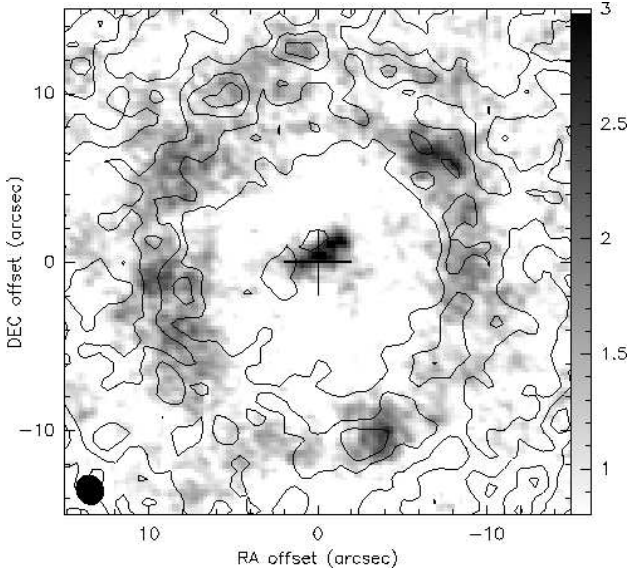


Fig. 8. $^{12}\text{CO}(1-0)$ contours as in Fig. 6 (left panel) superposed on the greyscale $^{12}\text{CO}(2-1)$ map that has been tapered, convolved to the same resolution, and corrected for primary beam attenuation, in units of $\text{Jy beam}^{-1} \text{km s}^{-1}$. The beam is plotted at lower left.

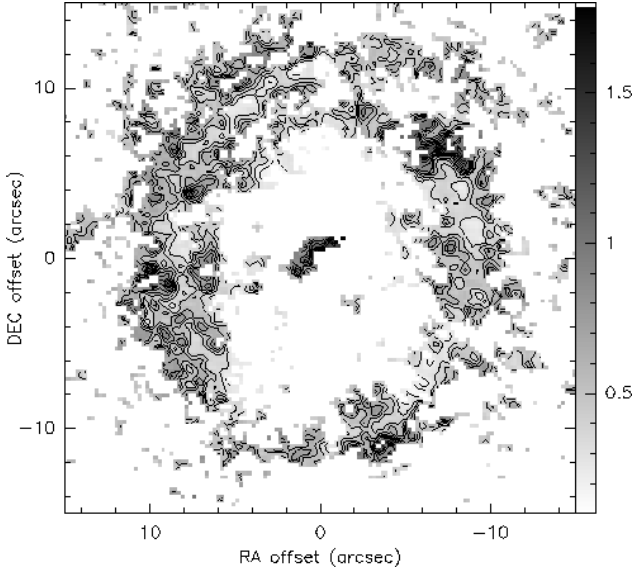


Fig. 9. Contours and greyscale of the $\text{CO}(2-1)/\text{CO}(1-0)$ ratio map. Contours run from 0.1 to 1.8 in steps of 0.1 in temperature units.

motions (visible on the minor-axis) is expected to change at corotation, while the tangential streaming (visible on the major-axis) does not change at corotation (e.g. Canzian 1993). Thus, we conclude (although with substantial uncertainty) that corotation occurs at $\sim 15''$ (3 kpc), consistent with the minor-axis p-v plot. This result will help constrain the pattern speed of the weak bar/oval which we discuss in Sect. 7.

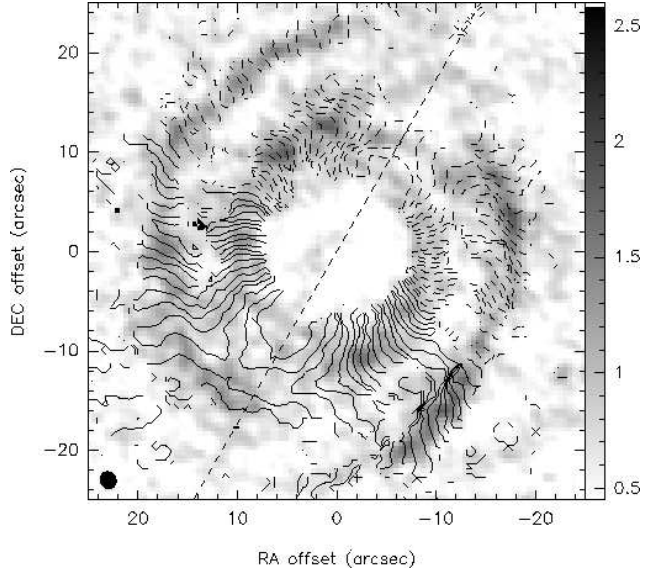


Fig. 10. Overlay of the integrated $^{12}\text{CO}(1-0)$ emission in grey scale, same as Fig. 6 (left panel), with the CO mean-velocity field in contours spanning the range -200 km s^{-1} to 200 km s^{-1} in steps of 10 km s^{-1} . The velocities are referred to $V_{\text{hel}} = 2813 \text{ km s}^{-1}$. Solid (dashed) lines are used for positive (negative) velocities. The dotted line indicates the major axis ($\text{PA} = 150^\circ$).

4.3. Dynamical mass

The peak velocity of $\sim 200 \text{ km s}^{-1}$ in the major-axis p-v diagram occurs at a radius of $\sim 7-8''$ (1.5 kpc). This value, when corrected for disk inclination (we adopt $i = 29.5^\circ$, see Table 1) by a factor $\sin i$, becomes 400 km s^{-1} . From the corrected peak velocity, we can estimate the dynamical mass within this radius: $M(R) = \alpha \times \frac{RV^2(R)}{G}$, where $M(R)$ is in M_\odot , R in kpc, and V in km s^{-1} . Assuming the most flattened disk-like distribution ($\alpha = 0.6$), gives a dynamical mass $M_{\text{dyn}} = 3.3 \times 10^{10} M_\odot$ within a diameter of ~ 3 kpc. Assuming a roughly flat rotation curve (see Sect. 7), this would imply a mass $M_{\text{dyn}} = 8.9 \times 10^{10} M_\odot$ within 4 kpc (roughly the radius of the PdBI primary beam for our $^{12}\text{CO}(1-0)$ observations). With a total molecular gas mass of $\sim 4 \times 10^9 M_\odot$ (see Sect. 4.1), we would thus estimate a molecular mass fraction of 4 – 5%.

5. Comparison with other wavelengths

It is instructive to compare the distribution of the molecular gas in the inner kpc of NGC 3147 with observations at other wavelengths. In particular, molecular clouds are thought to be the birth site of future generations of stars, and thus should be strongly connected to other emission tracing star formation, such as far-ultraviolet and warm dust emission.

5.1. The bar and the lopsided nucleus

The CO contours are superposed on the CFHT J -band image in Fig. 13. There is a weak bar/oval feature at a position angle $\text{PA} = 85^\circ$, just contained inside the inner CO ring. Only the NIR reveals this bar, since NGC 3147 is not classified optically

as a barred galaxy. Its late type (Sbc) corresponds to a non-dominating bulge, and the bar feature is likely not diluted by this bulge. The major axis orientation differs by 65° from the bar PA, which minimizes confusion due to projection effects.

Möllenhoff & Heidt (2001) have obtained *JHK* images of NGC 3147 with the 2.2 m telescope of the Calar Alto observatory using the MAGIC NICMOS3 camera, together with 40 other unbarred galaxies with low inclinations. They decomposed the images into bulge and disk components, and noticed that the bulge in NGC 3147 appears at a very different position angle than the disk; they concluded that the bulge must be triaxial, which was a rare feature in their sample. We have re-reduced their MAGIC *J* and *K'* images and the oval is present, similar to the feature seen in our CFHT images, although with noisier isophotes. Our kinematic data suggest that this bar may be the agent of the inflow that we discuss in Sect. 6,

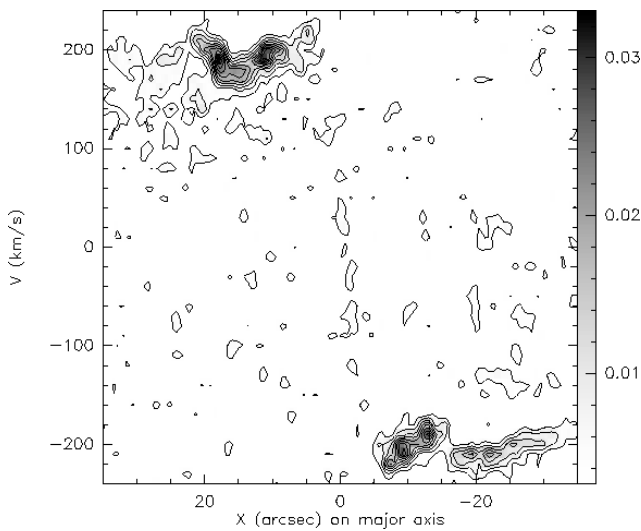


Fig. 11. $^{12}\text{CO}(1-0)$ position-velocity (p-v) diagram along the major axis of NGC 3147 using the whole velocity range $\pm 240 \text{ km s}^{-1}$. The coordinates of the center (0,0), the heliocentric velocity, and PA used are given in Table 1. Contour levels are from 3.2 to 32 mJy beam^{-1} in steps of $3.2 \text{ mJy beam}^{-1}$.

The ellipticity profile shown in Fig. 3 (see Sect. 2.4) helps us estimate the length of the bar/oval distortion. The ellipticity peaks at $\sim 5''$ (1 kpc), but the bar extends roughly to a radius of $\sim 7.5''$ (1.5 kpc). This is also seen in the *J*-band image (Fig. 13) where the bar is roughly $16''$ in diameter, and in the Fourier decomposition of the stellar potential discussed in Sect. 6. We therefore adopt a bar radius of $\sim 7.5''$ or ~ 1.5 kpc, although this estimate is subject to a rather large uncertainty, $\pm 30\%$.

The *J* – *K* image of NGC 3147 is shown in Fig. 14 with the $^{12}\text{CO}(2-1)$ integrated intensity overlaid as contours (see Sect. 4.1). Coincident with the nuclear CO emission, there is a clearly-defined non-axisymmetric structure of ~ 700 pc in size, which is bluer in *J* – *K* than the surrounding regions that are devoid of gas. This central asymmetric “blob” or “lopsided nucleus” could be the destination of the gas inflow that we discuss in Sect. 6.

5.2. The inner ring and the outer spiral

Fig. 15 displays the FUV image obtained with the *GALEX* satellite, described in Sect. 2.4. Inspection of Fig. 15 shows that NGC 3147 has a quite well-defined outer spiral structure, outside the range of our CO observations. There is also a compact nucleus with a central peak, surrounded by a roughly axisymmetric “plateau” of emission which breaks up into a pseudo ring at a radius of $\sim 20''$.

Fig. 16 shows the superposition of *GALEX* FUV image with the $^{12}\text{CO}(1-0)$ (left panel) and $^{12}\text{CO}(2-1)$ (right) integrated intensity contours. The cross shown in Fig. 15 is at the center of our CO observations, and coincides with the peak of the FUV nuclear emission. This agreement suggests that the FUV and CO emission are copatial in the nuclear region.

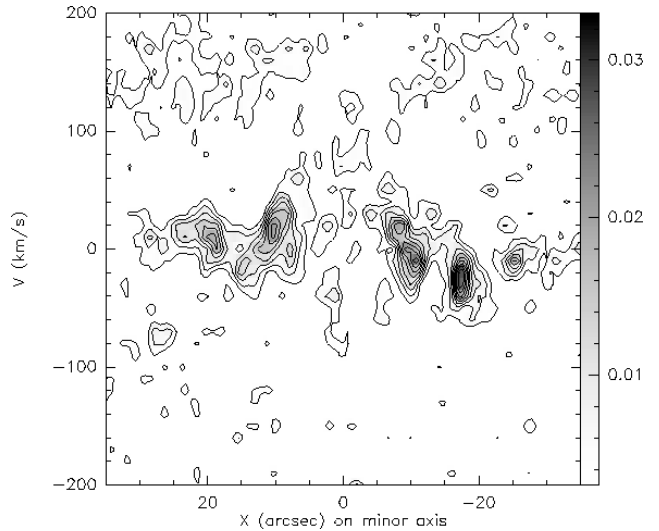


Fig. 12. $^{12}\text{CO}(1-0)$ position-velocity (p-v) diagram along the minor axis of NGC 3147 using the same velocity range, center, PA, and systemic velocity as for Fig. 11. Contour levels are from 2.8 to 28 mJy beam^{-1} in steps of $2.8 \text{ mJy beam}^{-1}$.

However, there is no clear ring in the FUV image. The inner $10''$ -radius CO ring is contained inside the circular region of the FUV emission, and the outer CO spiral ($20''$ -radius), at least its eastern part, has some overlap with the FUV spiral, but there are clear shifts between the two distributions. The $^{12}\text{CO}(2-1)$ emission (essentially the inner ring) also appears to settle inside the *GALEX* FUV inner “plateau” (Fig. 16).

The “outer spiral” in $^{12}\text{CO}(1-0)$ falls in the interarm “gap” in the *GALEX* image. Offsets between FUV and CO (or FIR and HI) emissions are not uncommon in grand design spiral galaxies, such as M 100 (Rand 1995; Sempere & García-Burillo 1997) and M 51 (Calzetti et al. 2005), and may relate to star-formation efficiency and timescale variations in response to a spiral density wave. The star formation and all related tracers are often located in different regions of the spiral arms: FUV emission is more prominent at the outer edge of the arms, where the dust extinction is low, while FIR and $\text{H}\alpha$ emission is stronger at the inner edge. However, in NGC 3147 we find CO in the middle of the inter-

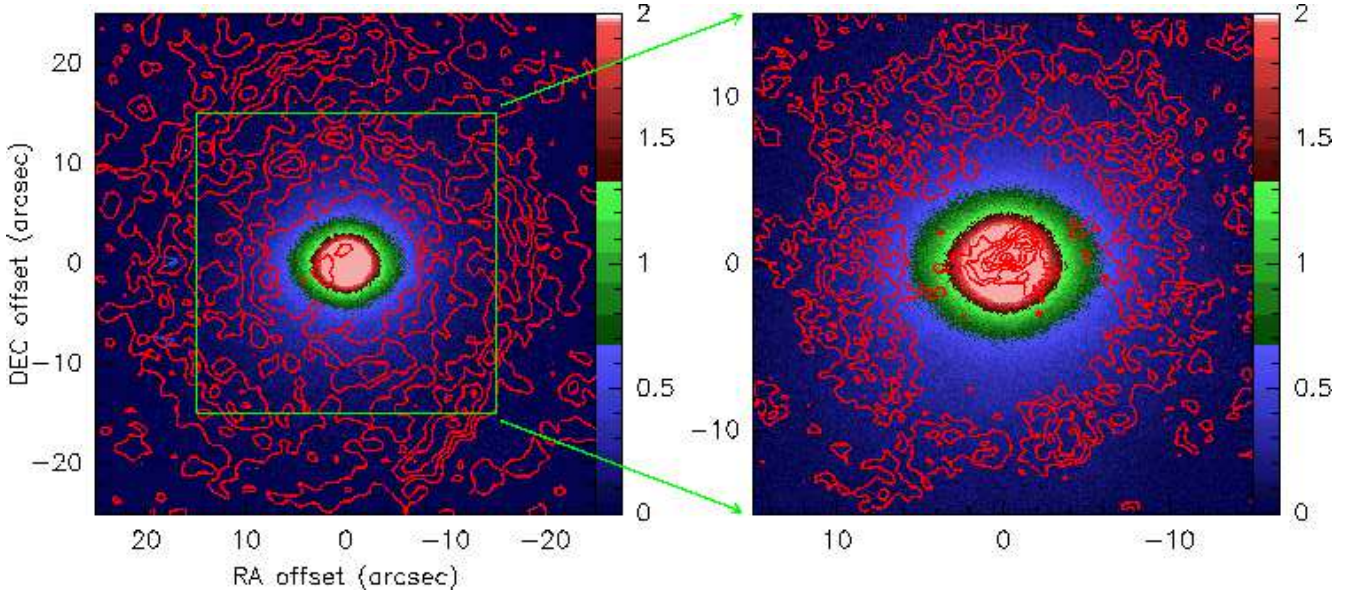


Fig. 13. *Left panel:* $^{12}\text{CO}(1-0)$ contours (0.6 to 2.6 by $0.35 \text{ Jy km s}^{-1} \text{ beam}^{-1}$) superposed on the near-infrared J image from the CFHT, shown in logarithmic levels. The central $50''$ are shown. *Right panel:* Same for $^{12}\text{CO}(2-1)$ contours (1.0 to 3.5 by $0.5 \text{ Jy km s}^{-1} \text{ beam}^{-1}$). The central $30''$ are shown.

arm region in the *GALEX* image, not at the inner or outer edge of the arm; this result is quite rare.

Unlike the FUV, the $8 \mu\text{m}$ “dust-only” image described in Sect. 2.4 shows an inner ring apparently associated with molecular gas.

Fig. 17 shows this image, which clearly exhibits an inner-ring structure at about $10''$ radius, together with a central peak. Such rings are frequently observed in barred galaxies with *Spitzer* (e.g. Regan et al. 2006). Fig. 18 shows the dust-only $8 \mu\text{m}$ image with the $^{12}\text{CO}(1-0)$ (left panel) and $^{12}\text{CO}(2-1)$ (right) intensity contours superposed. The ring visible at $8 \mu\text{m}$ corresponds to both the $^{12}\text{CO}(1-0)$ inner ring and the $^{12}\text{CO}(2-1)$ one. However, the outer $^{12}\text{CO}(1-0)$ spiral is slightly inside the corresponding structure in dust emission. This may be a similar phenomenon to that seen in the *GALEX* FUV image, where molecular gas peaks in the interarm regions as described above.

We can use the $8 \mu\text{m}$ dust-only image, together with the CO emission itself, to define the size and width of the inner gas (and dust) ring. The ring is rather broad, extending over roughly $2\text{--}3''$ in radius, or $\sim 500 \text{ pc}$. Measured to the middle of its width, the inner gas ring has a radius of $\sim 9\text{--}10''$ ($1.8\text{--}2 \text{ kpc}$), although it is slightly elongated, being longer along the horizontal axis. If instead we measure to the innermost portion of the ring, we find a radius of $\sim 7''\text{--}8''$ ($\sim 1.5 \text{ kpc}$). This uncertainty (20-30%) will influence our discussion in Sect. 7, where we will use the size of the ring in the context of the rotation curve to help constrain the pattern speed and location of the resonances that define the kinematics in NGC 3147.

5.3. Star formation

The agreement, where present, between the molecular gas distribution and the ultraviolet and infrared emission is consistent with on-going star formation within the molecular clouds. The

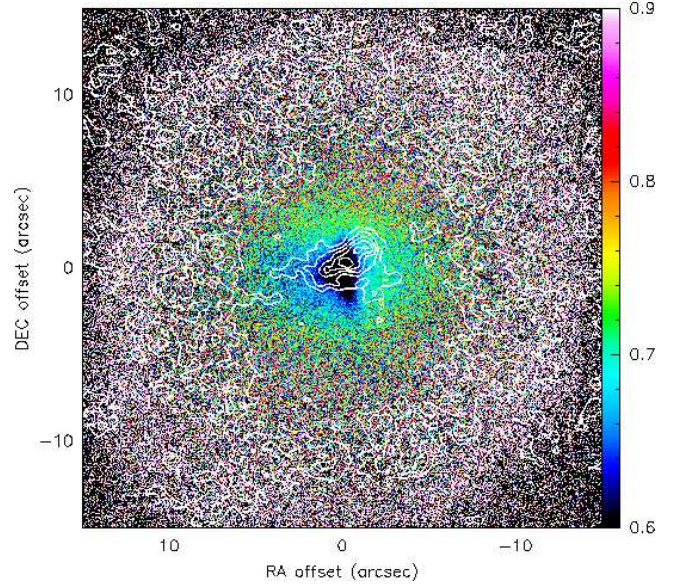


Fig. 14. The $J - K$ image from the CFHT with $^{12}\text{CO}(2-1)$ integrated intensity overlaid in contours (1.0 to 3.5 by $0.5 \text{ Jy km s}^{-1} \text{ beam}^{-1}$). North is up and east to the left.

star formation rate (SFR) can be computed from both UV and FIR emission using the calibrations given by Kennicutt (1998) for a $0.1\text{--}100 M_{\odot}$ Salpeter initial mass function:

$$\text{SFR} [M_{\odot} \text{ yr}^{-1}] = 1.4 \times 10^{-28} L_{UV} \quad (1)$$

where L_{UV} is the UV luminosity in $\text{ergs s}^{-1} \text{ Hz}^{-1}$ over the wavelength range $1500\text{--}2800 \text{ \AA}$, and

$$\text{SFR} [M_{\odot} \text{ yr}^{-1}] = 4.5 \times 10^{-44} L_{FIR} \quad (2)$$

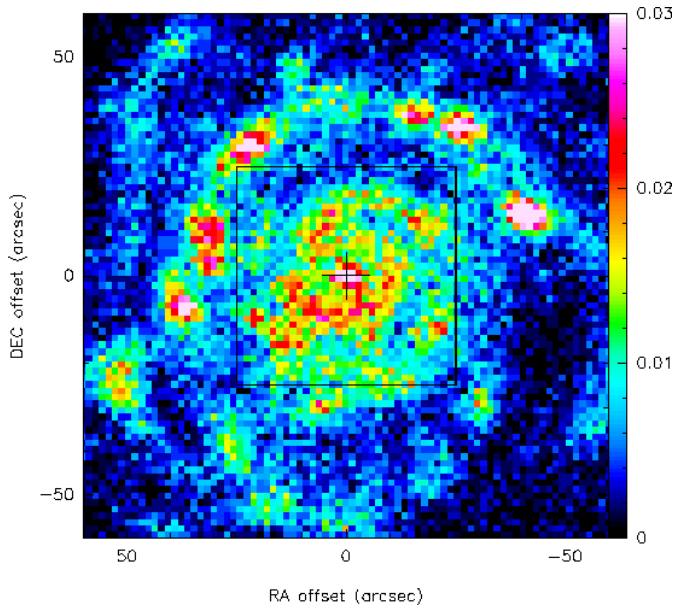


Fig. 15. *GALEX* FUV sky subtracted image of NGC 3147. The central 120'' of the galaxy are shown. The box shows the central 50'', field of view of our ^{12}CO observations.

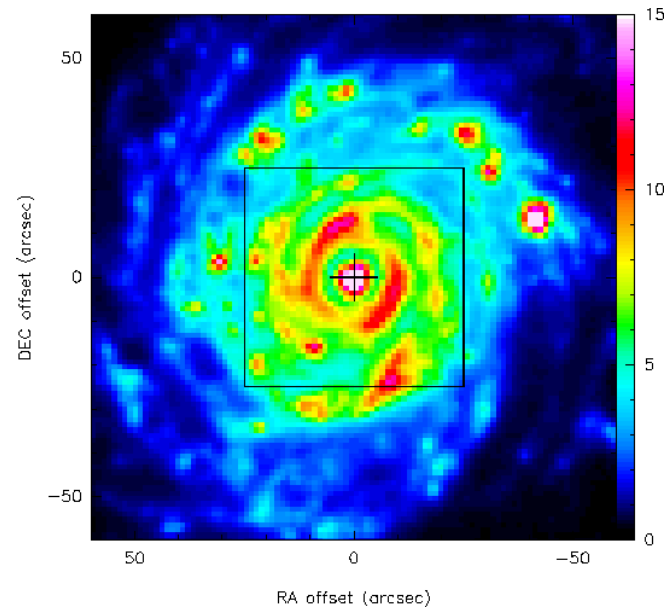


Fig. 17. *Spitzer/IRAC* “dust-only” image at $8\ \mu\text{m}$ of NGC 3147. The central 120'' of the galaxy are shown. The box shows the central 50'', field of view of our ^{12}CO observations.

where L_{FIR} , expressed in ergs s^{-1} , refers to the total infrared luminosity integrated over the entire mid and far-IR spectrum (8-1000 μm). We first compute the UV luminosity from the *GALEX* map inside the FOV of 42'', to better separate the SFR in the PdBI FOV from the total, and find a SFR $\sim 1\ \text{M}_{\odot}\ \text{yr}^{-1}$.

We then use the *Spitzer* MIPS images available from the archive to estimate how much FIR flux falls within the FOV of the PdBI primary beam compared to the total integrated over the much larger *IRAS* beams. Rough measurements give a fraction of $\sim 12\%$ for $160\ \mu\text{m}$ and $\sim 22\%$ for $24\ \mu\text{m}$ (the $70\ \mu\text{m}$ image is not available). We then estimate the FIR luminosity by scaling

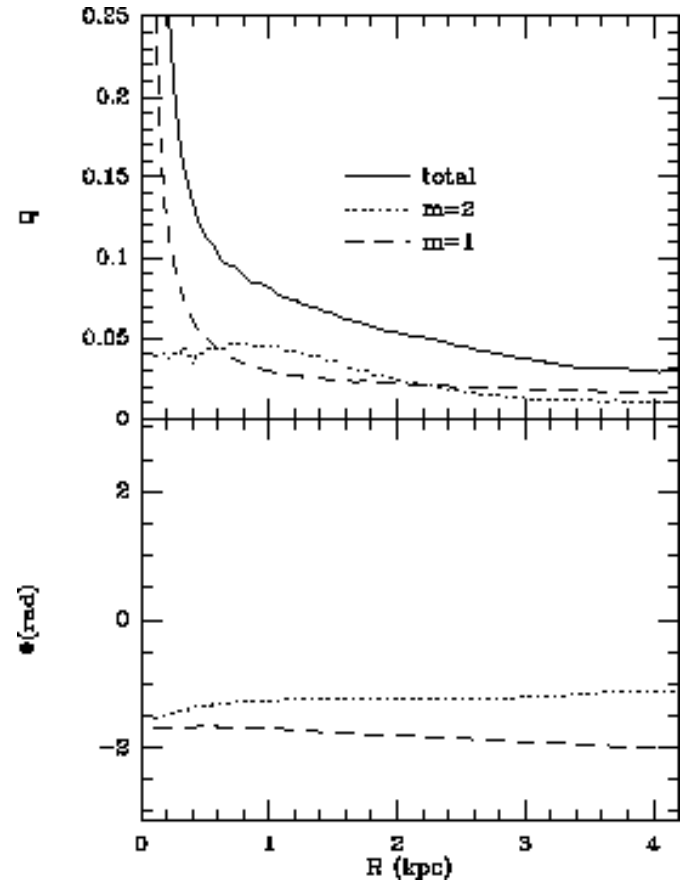


Fig. 19. Strengths (Q_1 , Q_2 , and total Q_T) and phases (ϕ_1 and ϕ_2) of the $m = 1$ and $m = 2$ Fourier components of the stellar potential inside a field of 48'' in diameter ($r < 4.6\ \text{kpc}$).

the *IRAS* $100\ \mu\text{m}$ and $60\ \mu\text{m}$ fluxes by 12% and 17%², respectively. This gives 1.39 Jy at $60\ \mu\text{m}$ and 3.55 Jy at $100\ \mu\text{m}$, which results in an estimate for the SFR of $\sim 0.8\ \text{M}_{\odot}\ \text{yr}^{-1}$, similar to that obtained from *GALEX*.

The compatibility between the two estimations of SFR (from UV and FIR) means that there is not significant obscuration, which is probably due to the nearly face-on view of the galaxy.

The SFR per unit area inferred from these values is $0.016\ \text{M}_{\odot}\ \text{yr}^{-1}\ \text{kpc}^{-2}$, high for spiral disks but similar to, although slightly lower than, typical values for IR-selected circumnuclear starbursts (Kennicutt 1998). Moreover, given the gas mass we derived in Sect. 4.1 and the correlations shown in Kennicutt (1998), the global star-formation efficiency within the inner 8 kpc is low, $\sim 1\%$ rather than the more typical value of $\sim 10\%$. On the other hand, the molecular gas is concentrated into well-defined structures; more than half the molecular mass is found in the inner ring alone (see Sect. 4.1). If we consider only the molecular gas in the inner ring, the gas surface density is $\sim 320\ \text{M}_{\odot}\ \text{pc}^{-2}$, roughly 4 times higher than we obtain by averaging over the entire FOV. Nevertheless, it is significantly lower than that in M 51 spiral arms (Henry et al. 2003).

² 17% is a rough interpolation of the central concentration we would expect at $60\ \mu\text{m}$, given the more compact emission at $24\ \mu\text{m}$ and the more extended emission at $160\ \mu\text{m}$.

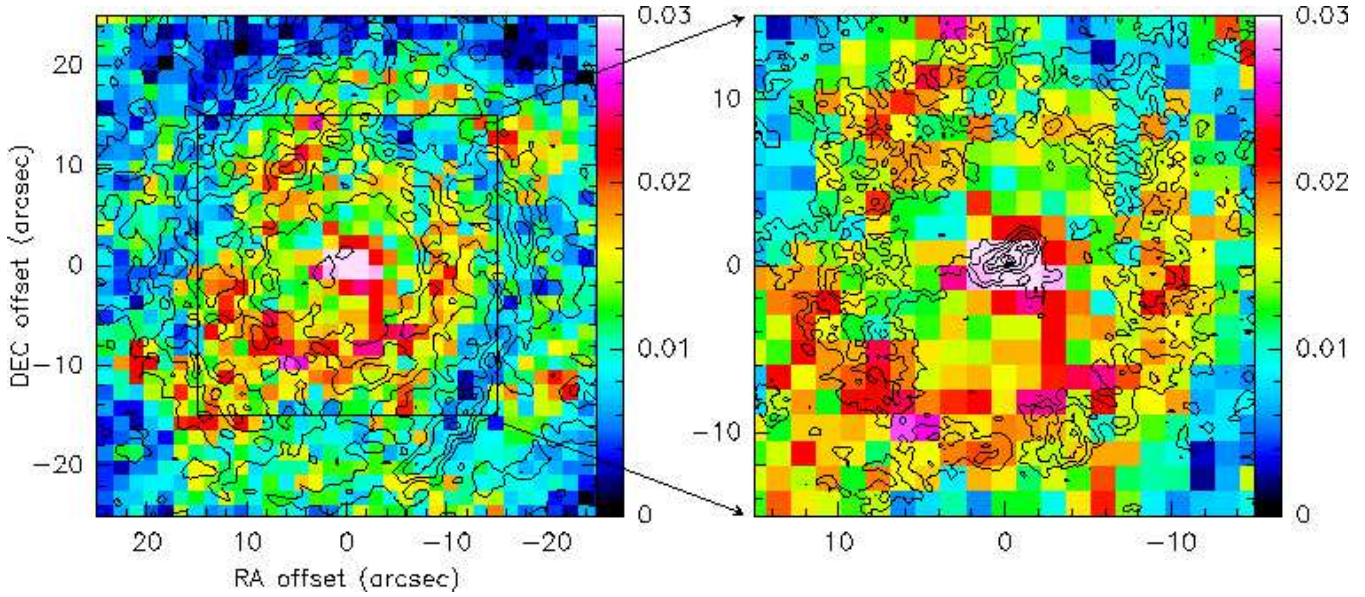


Fig. 16. *Left panel:* $^{12}\text{CO}(1-0)$ contours (0.6 to 2.6 by $0.35 \text{ Jy km s}^{-1} \text{ beam}^{-1}$) superposed on the *GALEX* FUV image of NGC 3147, shown in logarithmic levels. The central $50''$ are shown. *Right panel:* Same for $^{12}\text{CO}(2-1)$ contours (1.0 to 3.5 by $0.5 \text{ Jy km s}^{-1} \text{ beam}^{-1}$). The central $30''$ are shown.

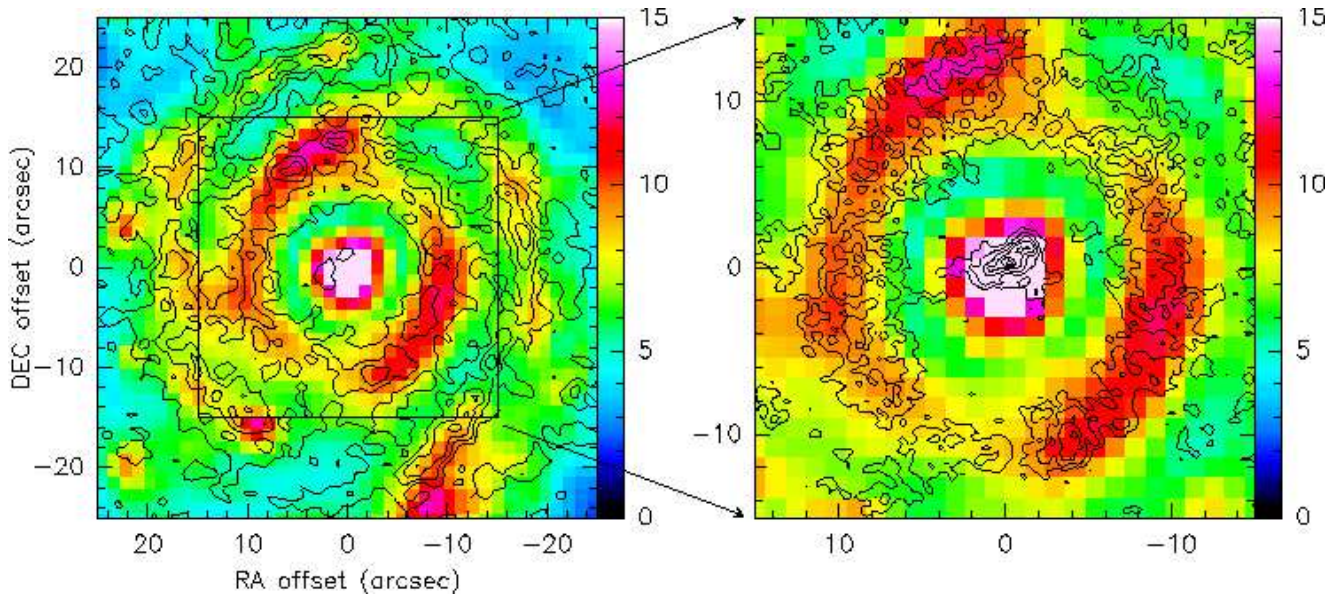


Fig. 18. *Left panel:* $^{12}\text{CO}(1-0)$ contours (0.6 to 2.6 by $0.35 \text{ Jy km s}^{-1} \text{ beam}^{-1}$) superposed on the $8 \mu\text{m}$ “dust-only” (*Spitzer/IRAC*) image of NGC 3147, shown in logarithmic levels. The central $50''$ are shown. *Right panel:* Same for $^{12}\text{CO}(2-1)$ contours (1.0 to 3.5 by $0.5 \text{ Jy km s}^{-1} \text{ beam}^{-1}$). The central $30''$ are shown.

6. Computation of the torques

6.1. Evaluation of the gravitational potential

As described in previous papers (e.g., García-Burillo et al. 2005), we assume that NIR images can give us the best approximation for the total stellar mass distribution, being less affected than optical images by dust extinction or by stellar population biases. We here recall the essential definitions and assumptions.

The *J*-band image was first deprojected according to the angles $\text{PA} = 150^\circ$ and $i = 29.5^\circ$. We have not deprojected the bulge separately, since we do not know its actual flattening, but

because the galaxy is of late type (Sbc), it does not have a large contribution. The image is completed in the vertical dimension by assuming an isothermal plane model with a constant scale height, equal to $\sim 1/12$ th of the radial scale-length of the image. The potential is then derived by a Fourier transform method, assuming a constant mass-to-light (M/L) ratio. The M/L value is selected to reproduce the observed CO rotation curve. The potential was also calculated from the lower-resolution MAGIC images, which have a much larger field-of-view ($162''$). The same results are obtained, and the potential is shown to be axisymmetric at large radii. Beyond a radius of $20''$, the mass

density is set to 0, thus suppressing any spurious $m = 4$ terms; this is sufficient to compute the potential over the PdB $^{12}\text{CO}(1-0)$ primary beam.

For the non-axisymmetric part, the potential $\Phi(R, \theta)$ is then decomposed in the different m -modes:

$$\Phi(R, \theta) = \Phi_0(R) + \sum_{m=1}^{\infty} \Phi_m(R) \cos(m\theta - \phi_m(R))$$

where $\Phi_m(R)$ and $\phi_m(R)$ represent the amplitude and phase of the m -mode.

The strength of the m -Fourier component, $Q_m(R)$ is defined as $Q_m(R) = m\Phi_m/R|F_0(R)|$, i.e. by the ratio between tangential and radial forces (e.g. Combes & Sanders 1981). The strength of the total non-axisymmetric perturbation is defined by:

$$Q_T(R) = \frac{F_T^{\max}(R)}{F_0(R)}$$

where $F_T^{\max}(R)$ represents the maximum amplitude of the tangential force and $F_0(R)$ is the mean axisymmetric radial force. Fig. 19 displays these Q values as a function of radius for NGC 3147. A bar ($m = 2$) can be seen clearly, with a peak radius of ~ 1 kpc ($5''$), and a total extent of 1.5 kpc ($7.5''$) in radius. These dimensions are similar to those inferred from the ellipticity distribution discussed in Sect. 5.1, and strengthen our conclusion that this structure is “bar-like”. There is also an asymmetry in the $m = 2$ profile towards the center. The lopsidedness has a correspondence in the gas morphology described in Sect. 4.1 and the $J - K$ image discussed in Sect. 2.4. The bar is regular in phase, but its strength is relatively modest.

6.2. Evaluation of gravity torques

After having calculated the forces per unit mass (F_x and F_y) from the derivatives of $\Phi(R, \theta)$ on each pixel, the torques per unit mass $t(x, y)$ can be computed by:

$$t(x, y) = x F_y - y F_x$$

The torque map is oriented according to the sense of rotation in the plane of the galaxy. The combination of the torque map and the gas density Σ map then allows us to derive the net effect on the gas at each radius. The gravitational torque map weighted by the gas surface density $t(x, y) \times \Sigma(x, y)$, normalized to its maximum value, is shown in Figs. 20 and 21 for $\text{CO}(1-0)$ and $\text{CO}(2-1)$, respectively.

To estimate the radial gas flow induced by the torques, we first compute the torque per unit mass averaged over azimuth, using $\Sigma(x, y)$ as the actual weighting function, i.e.:

$$t(R) = \frac{\int_{\theta} \Sigma(x, y) \times (x F_y - y F_x)}{\int_{\theta} \Sigma(x, y)}$$

By definition, $t(R)$ represents the time derivative of the specific angular momentum L of the gas averaged azimuthally, i.e., $t(R) = dL/dt|_{\theta}$. To derive dimensionless quantities, we normalize this variation of angular momentum per unit time to the angular momentum at this radius and to the rotation period. We

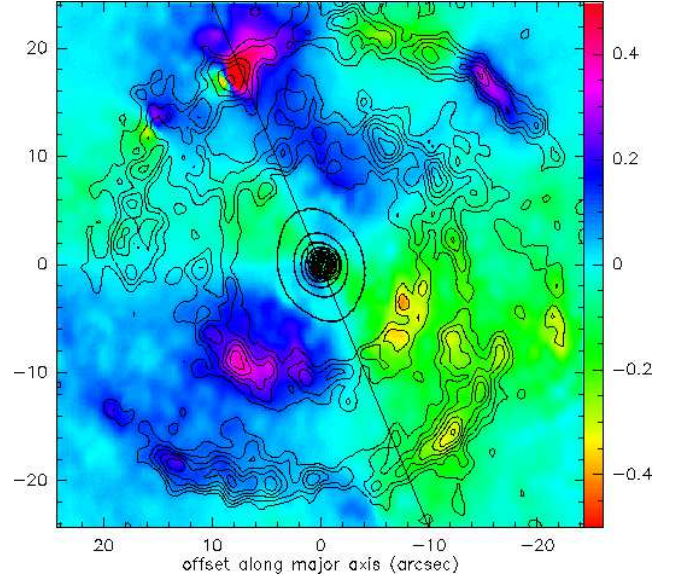


Fig. 20. $\text{CO}(1-0)$ contours overlaid on the gravitational torque map ($t(x, y) \times \Sigma(x, y)$, as defined in text) in the center of NGC 3147. The torque map (grey/color scale) is normalized to the maximum absolute value of the torques. The derived torques change sign as expected in a *butterfly* diagram, delineating four quadrants. The orientation of quadrants follow the bar orientation in NGC 3147. In this deprojected picture, the major axis of the galaxy is oriented parallel to the abscissa. The line reproduces the mean orientation of the bar (PA = 20° on the deprojected image and 85° on the projected one).

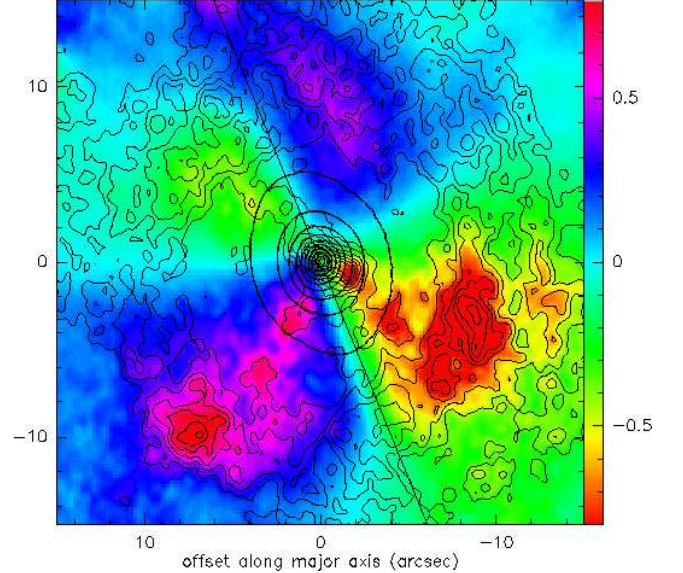


Fig. 21. Same as Fig. 20 for the $^{12}\text{CO}(2-1)$ emission taken as a tracer of gas surface density.

then estimate the efficiency of the gas flow as the average fraction of the gas specific angular momentum transferred in one rotation (T_{rot}) by the stellar potential, as a function of radius, i.e., by the function $\Delta L/L$ defined as:

$$\frac{\Delta L}{L} = \frac{dL}{dt} \Big|_{\theta} \times \frac{1}{L} \Big|_{\theta} \times T_{rot} = \frac{t(R)}{L_{\theta}} \times T_{rot}$$

where L_θ is assumed to be well represented by its axisymmetric estimate, i.e., $L_\theta = R \times v_{rot}$. The $\Delta L/L$ curves for NGC 3147 derived from the CO(1–0) and the CO(2–1) data are displayed in Figs. 22.

The gravitational torque maps in Fig. 20 show that the derived torques change sign following a characteristic 2D *butterfly* pattern. The CO contours reveal that for the material in the inner ring (radius 2 kpc, $10''$), part of the gas is trailing the bar, while part of the gas is leading it. The observed gas distribution is representative of the time spent by a molecular cloud on a typical orbit at this location. The azimuthal average of the torques shown in Fig. 22 suggests that the torques are predominantly negative inside a radius of ~ 2 kpc, while they become zero or positive outside.

If the near side is the northeast side, the rotation sense of the galaxy is counterclockwise, and the whole spiral structure is trailing with respect to the rotation. In the spiral structure winding into the outer $^{12}\text{CO}(1-0)$ ring, the torques almost cancel out on average but are still predominantly positive. Inside the inner ring ($r < 2$ kpc), however, the dominating torques are negative, although weak in absolute value. The $^{12}\text{CO}(2-1)$ emission is more clumpy, and our map suffers from lower sensitivity; there is relatively more emission in the central part. Although the emission is spread over three quadrants in the center, the negative torques are still predominant there (Fig. 21). The negative torques there are due to the central asymmetric CO distribution, mainly the nuclear component, at radii inside 3–4''. The component is resolved in $^{12}\text{CO}(2-1)$, and is not aligned with the nuclear bar, but rather shifted to the leading side; therefore, negative torques dominate.

7. Discussion

We find that the two molecular structures (inner ring and outer spiral), in addition to a central peak of $^{12}\text{CO}(2-1)$ emission, dominate the CO map of NGC 3147's inner region. The inner ring coincides with the ring in the dust-only $8\mu\text{m}$ image, and the lopsided central peak falls at the same position as the asymmetric nuclear structure in the $J-K$ map. These features are not present in the stars (e.g., J band, IRAC $3.6\mu\text{m}$, and *GALEX*), but are rather features of the ISM. On the other hand, the outer spiral also appears in the stars as shown by the *GALEX* image; however, there is an offset between them, as the CO emission falls in the interarm region relative to the outer spiral (see Fig. 16).

A probable explanation is that the CO outer spiral is not a permanent structure but is transient. The gas participates in a spiral wave and forms stars, and then the newly formed stars decouple from the gas component. The young stars heat only the dust present at their location, while the bulk of the gas has moved to another density condensation. The inward migration of the dense gas with respect to the initial resonance has for been discussed by, e.g., Regan & Teuben (2003). This phenomenon, because it is very transient, is statistically rarely encountered. In this scenario, the CO clouds would not trace stars of the same age as those that have heated the dust observable at $8\mu\text{m}$ or of those whose emission is detected in the FUV, but rather they will be the birth site of future stellar generations.

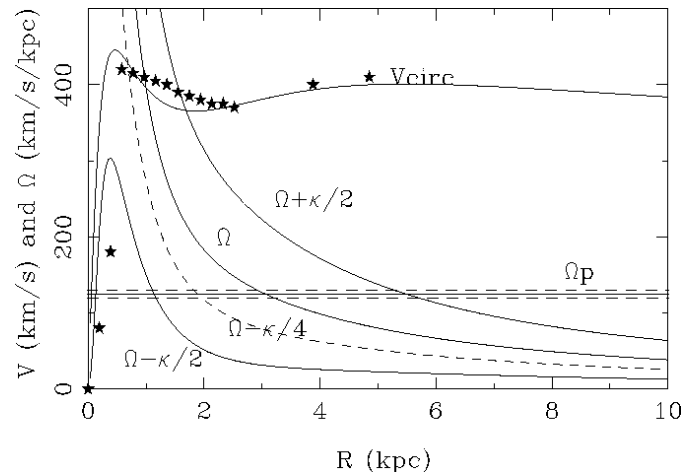


Fig. 23. Model rotation curve and derived frequencies Ω , $\Omega - \kappa/2$, and $\Omega + \kappa/2$, for NGC 3147. The star symbols are the data derived from the CO kinematics, deprojected with an inclination of $i = 29.5^\circ$. The horizontal line corresponds to $\Omega_p = 125 \text{ km s}^{-1} \text{ kpc}^{-1}$.

For the torques computation, we interpret the results by identifying the resonances with the bar. Let us note that CO resonant rings have already been observed in weakly barred galaxies, where the bar is inconspicuous in the optical (e.g., NGC 5005, NGC 7217: Sakamoto et al. 2000; Combes et al. 2004). The rotation curve derived from the CO kinematics is rather peaked in the center, and corresponds well to the gravitational model obtained from the NIR image. Both are fitted by an axisymmetric mass model, with a rotation curve as shown in Fig. 23, which allows us to derive the characteristic dynamical frequencies.

If the stellar bar ends at or just inside its ultra-harmonic resonance (UHR), as is canonical for bar dynamics, this means that the pattern speed of the bar would be roughly $\Omega_p = 120 - 130 \text{ km s}^{-1} \text{ kpc}^{-1}$, corresponding to a bar with one or two inner Lindblad resonances, as is common. The presence of these ILRs is not certain, however, given the possible non-circular motions in the bar. The inner CO ring would then correspond to the UHR ($r = 2$ kpc, $10''$) just inside corotation, which we estimated to be at a radius of $\sim 15''$ (3 kpc) in Sect. 4.2. The measurements of the inner ring radius and bar length suggest that the bar/oval ends roughly at the onset of the inner ring. However, the considerable uncertainties of these measurements and the finite width of the ring lead to an uncertainty in the pattern speed Ω_p of the bar.

The outer CO spiral corresponds to the spiral structure emerging from the bar, beyond its corotation. The pitch angle of these spiral arms is quite small, as is expected for a weak bar. In this scenario, the gas in the inner CO ring is inside corotation; due to the negative torques there, the gas loses angular momentum and is therefore flowing inwards. Due to the weak bar, the rate of inflow is relatively low, with a time-scale of about 5 rotations (Fig. 22).

The amount of gas flowing inwards is consistent with what might be needed to fuel the Seyfert 2 nucleus. The gas surface density in the central kiloparsec is about $10 \text{ M}_\odot \text{ pc}^{-2}$; if the

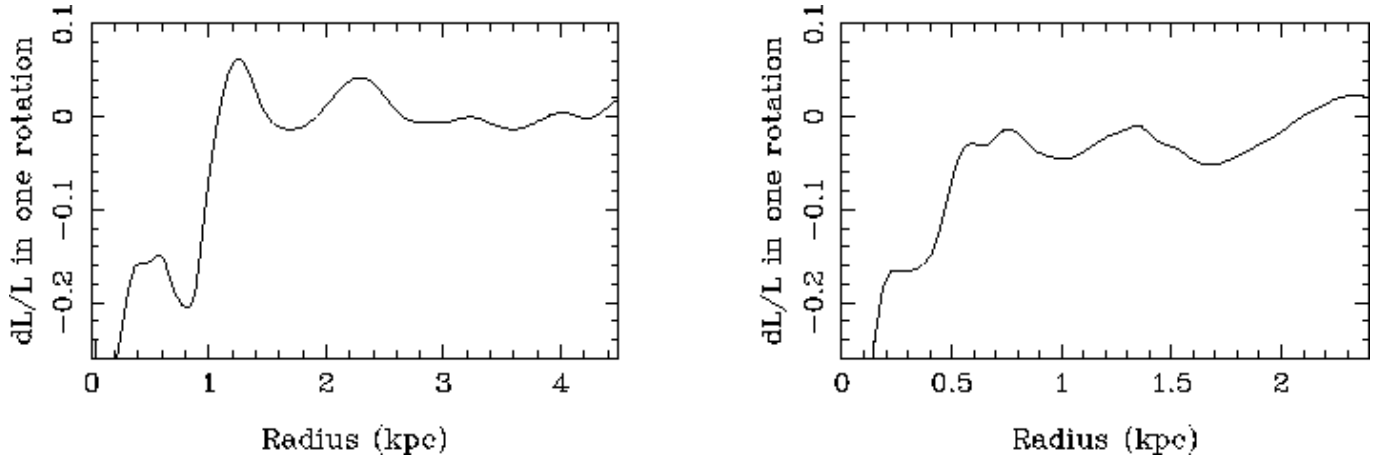


Fig. 22. The torque, or more precisely the fraction of the angular momentum transferred from/to the gas in one rotation $-dL/L$ is plotted for $^{12}\text{CO}(1-0)$ (left) and $^{12}\text{CO}(2-1)$ (right).

gas at 1 kpc from the center falls in within 5 dynamical time-scales (of ~ 20 Myr), then the feeding rate is about $0.5 M_{\odot} \text{ yr}^{-1}$. Assuming a mass-to-energy conversion efficiency of $\epsilon \sim 10\%$ ($L = dM/dt c^2 \epsilon$), then a luminosity of order $3 \times 10^{45} \text{ erg s}^{-1}$ is accounted for, more than enough for this low-luminosity AGN.

The spatial resolution of the CO maps is not yet sufficient to determine more precisely whether the gas is actually feeding the AGN, but we can at least conclude that we are observing the gas inflow into the ~ 100 – 200 pc scale circumnuclear region.

8. Conclusions

The molecular gas in the Seyfert 2 galaxy NGC 3147 has been mapped with high resolution ($1''.9 \times 1''.6$ Gaussian beam for the $^{12}\text{CO}(1-0)$ line) inside a radius of $25''$ (~ 5 kpc). The CO emission shows a central peak (mainly in $^{12}\text{CO}(2-1)$) and a ring at distance of 2 kpc. In $^{12}\text{CO}(1-0)$ also an outer spiral at distance of 4 kpc is detected. The observed CO has a mean line intensity ratio $I_{21}/I_{10} \sim 0.7$, consistent with the optically thick emission expected in the nuclei of spiral galaxies, and broadly regular kinematics with some evidence for local non-circular motions.

Comparing the molecular gas distribution with tracers of star formation, we find that central emission and the inner CO ring coincide well with the FUV (*GALEX*) and $8 \mu\text{m}$ (*Spitzer*) emission, while the outer CO spiral structure/ring is instead located within an interarm interval detected by *GALEX* and *Spitzer*. We interpret this partial disagreement as due to the transient nature of the outer CO ring. It would be a structure in re-condensation that traces a future stellar generation, but is decoupled from those that have heated the dust observable at $8 \mu\text{m}$ or from whose emission is detected in the FUV.

With a NIR image obtained with the Canada-France-Hawaii Telescope, we have identified the presence of a weak bar in NGC 3147, a galaxy classified as non-barred in the optical. This stellar bar acting on the gas produces gravity torques. A portion of the gas present in the inner $^{12}\text{CO}(1-0)$ ring is trailing the bar, while part of the gas leads it. The gravity torques are negative inside a radius of ~ 2 kpc, while they become zero or positive outside. In the outer $^{12}\text{CO}(1-0)$ spiral the torques almost cancel out on average, but are positive. In the more

clumpy inner $^{12}\text{CO}(2-1)$ ring, the predominant torques are negative. We interpret these results by identifying the resonances with the bar. The inner CO ring would correspond to the ultra-harmonic resonance ($r = 2$ kpc) just inside corotation, and the outer CO spiral to the spiral structure emerging from the bar, beyond its corotation, which we estimate is located at ~ 3 kpc. In the inner CO ring, the gas is inside corotation due to the negative torques there; it loses angular momentum and is flowing inwards.

NGC 3147 is not the first case in the NUGA sample where inflowing gas has been found: NGC 2782 (Hunt et al. 2008), and NGC 6574 (Lindt-Krieg et al. 2008) also show this feature. However, only NGC 2782 has a strong and significant inflow, due to a nuclear bar embedded in the primary one and to gas aligned with the nuclear bar. The amount of inflowing gas in NGC 3147, quantified from the gravity torques computation, is modest but could still be sufficient to feed the Seyfert 2 nucleus at a rate of about $0.5 M_{\odot} \text{ yr}^{-1}$. Although higher spatial resolution is needed to determine whether the gas is actually feeding the AGN, we are observing the gas inflow to the ~ 100 – 200 pc central region.

Acknowledgements. The authors would like to thank the anonymous referee, whose comments have been very instructive and useful for improving the original version of the paper. We thank the scientific and technical staff at IRAM for their work in making our 30 m and PdBI observations possible. V. Casasola is pleased to acknowledge the hospitality and stimulating environment provided by the Observatoire de Paris-LERMA, where part of the work on this paper was done during her stay in Paris, thanks to the EARA agreement. In this work, we have made use of *MAST/GALEX* images and the *Spitzer* archive.

References

- Bettoni, D., Galletta, G., & García-Burillo, S. 2003, *A&A*, 405, 5
- Bianchi, L., Madore, B., Thilker, D., Gil de Paz, A., Martin, C., & The *GALEX* Team 2003a, *The Local Group as an Astrophysical Laboratory*, 10

- Bianchi, L., Madore, B., Thilker, D., Gil de Paz, A., & GALEX Science Team 2003b, *Bulletin of the American Astronomical Society*, 35, 1354
- Bianchi, S., Corral, A., Panessa, F., Barcons, X., Matt, G., Bassani, L., Carrera, F. J., & Jiménez-Bailón, E. 2008, *MNRAS*, 108
- Boone, F., et al. 2007, *A&A*, 471, 113
- Braine, J., & Combes, F. 1992, *A&A*, 264, 433
- Braine, J., Combes, F., Casoli, F., et al.: 1993, *A&AS*, 97, 887
- Calzetti, D., et al. 2005, *ApJ*, 633, 871
- Canzian, B. 1993, *ApJ*, 414, 487
- Casoli, F., Dickey, J., Kazes, I., Boselli, A., Gavazzi, G., & Jore, K. 1996, *A&AS*, 116, 193
- Combes, F., & Sanders, R. H. 1981, *A&A*, 96, 164
- Combes, F. 2001, *Advanced Lectures on the Starburst-AGN*, 223
- Combes, F., Garca-Burillo, S.; Boone, F.; et al. 2004, *A&A*, 414, 857, (NUGA II)
- Friedli, D., & Martinet, L. 1993, *A&A*, 277, 27
- García-Burillo, S., Sempere, M. J., Combes, F., Hunt, L. K., & Neri, R. 2000, *A&A*, 363, 869
- García-Burillo, S., et al. 2003, *A&A*, 407, 485, (NUGA I)
- García-Burillo, S., Combes, F., Schinnerer, E., Boone, F., & Hunt, L. K. 2005, *A&A*, 441, 1011, (NUGA IV)
- Gil de Paz, A., Madore, B. F., Boissier, S., & GALEX Science Team 2004, *Bulletin of the American Astronomical Society*, 36, 1410
- Guilloteau, S., & Lucas, R. 2000, *Imaging at Radio through Submillimeter Wavelengths*, 217, 299
- Heckman, T. M., Smith, E. P., Baum, S. A., et al.: 1986, *ApJ*, 311, 526
- Heckman, T. M., Blitz, L., Wilson, A. S., Armus, L., & Miley, G. K. 1989, *ApJ*, 342, 735
- Helfer, T. T., Thornley, M. D., Regan, et al.: 2003, *ApJS*, 145, 259
- Helou, G., et al. 2004, *ApJS*, 154, 253
- Henry, A. L., Quillen, A. C., & Gutermuth, R. 2003, *AJ*, 126, 2831
- Ho, L. C., Filippenko, A. V., & Sargent, W. L. W. 1997, *ApJS*, 112, 315
- Hunt, L. K., et al. 2008, *A&A*, 482, 133 (NUGA IX)
- Jogee, S. 2006, *Physics of Active Galactic Nuclei at all Scales*, 693, 143, (astro-ph/0408383)
- Kennicutt, R. C., Jr. 1998, *ARA&A*, 36, 189
- Kohno, K., Ishizuki, S., Matsushita, S., Vila-Vilaro, B., Kawabe, R.: 2003, *PASJ* 55, L1
- Krips, M., Eckart, A., Neri, R., Schödel, R., Leon, S., Downes, D., García-Burillo, S., & Combes, F. 2006, *A&A*, 446, 113
- Krips, M., Eckart A., Krichbaum T.P. et al. 2007a, *A&A*, 464, 553, (NUGA V)
- Krips, M., Neri R., García-Burillo, S.: 2007b, *A&A* 468, L63, (NUGA VI)
- Lindt-Krieg, E., Eckart, A., Neri, R., Krips, M., Pott, J.-U., García-Burillo, S., & Combes, F. 2008, *A&A*, 479, 377, (NUGA VIII)
- Möllenhoff C., Heidt J.: 2001, *A&A* 368, 16
- Nagar, N. M., Falcke, H., Wilson, A. S., & Ulvestad, J. S. 2002, *A&A*, 392, 53
- Pahre, M. A., Ashby, M. L. N., Fazio, G. G., & Willner, S. P. 2004, *ApJS*, 154, 229
- Rand, R. J. 1995, *AJ*, 109, 2444
- Roberts, T. P., & Warwick, R. S. 2000, *MNRAS*, 315, 98
- Regan, M. W., Thornley, M. D., Helfer, T. T. et al.: 2001, *ApJ*, 561, 218
- Regan, M. W., Teuben P., 2003, *ApJ*, 582, 723
- Regan, M. W., Thornley, M. D., Vogel S.N., et al.: 2006, *ApJ*, 652, 1112
- Rigaut, F., Salmon, D., Arsenault, R. et al. 1998, *PASP*, 110, 152
- Sakamoto, K., Okumura, S. K., Ishizuki, S., & Scoville, N. Z. 1999, *ApJS*, 124, 403
- Sakamoto, K., Baker A.J., Scoville N.Z.: 2000, *ApJ*, 533, 149
- Schinnerer, E., Eckart, A., & Tacconi, L. J. 2000a, *ApJ*, 533, 826
- Schinnerer, E., Eckart, A., Tacconi, L. J., Genzel, R., & Downes, D. 2000b, *ApJ*, 533, 850
- Sempere, M. J., & García-Burillo, S. 1997, *A&A*, 325, 769
- Shu, F. H., Tremaine, S., Adams, F. C., & Ruden, S. P. 1990, *ApJ*, 358, 495
- Solomon, P. M., & Barrett, J. W. 1991, *Dynamics of Galaxies and Their Molecular Cloud Distributions*, 146, 235
- Terashima, Y., & Wilson, A. S. 2003, *ApJ*, 583, 145
- Ulvestad, J. S., & Ho, L. C. 2001, *ApJ*, 562, L133
- Vila-Vilaró, B., Taniguchi, Y., & Nakai, N. 1998, *AJ*, 116, 1553
- Young, J. S., Xie, S., Tacconi, L., et al. 1995, *ApJS*, 98, 219